STUDY OF THE PASSIVITY OF UNS S32003 LEAN DUPLEX STAINLESS STEEL IN CHLORIDE CONTAINING ENVIRONMENTS

A Thesis

Presented to

The Graduate Faculty of The University of Akron

In Partial Fulfilment

of the Requirements for the Degree

Master of Science

Javier E. Esquivel Guerrero

December, 2015

STUDY OF THE PASSIVITY OF UNS S32003 LEAN DUPLEX STAINLESS STEEL IN CHLORIDE CONTAINING ENVIRONMENTS

Javier E. Esquivel Guerrero

Thesis

Approved:	Accepted:
Advisor Dr. Homero Castañeda-Lopez	Dean of the College Dr. Rex Ramsier
Committee Member Dr. Qixin Zhou	Dean of the Graduate School Dr. Chand Midha
Committee Member Dr. Rajeev Gupta	Date
Department Chair Dr. H. Michael Cheung	

ABSTRACT

In this work the study of the passivity of UNS S32003 was carried out utilizing different electrochemical, microscopy and surface characterization techniques. Optical profilometry, SEM and direct current electrochemical tests were used to support the materials characterization. A high resolution quantitative analysis from x-ray photo-electron spectroscopy (XPS) data was performed to quantify the interfacial properties of the metallic substrate; the experimental results were used to develop a theoretical approach by assuming a point defect model (PDM). This model was adapted and optimized based on electrochemical impedance spectroscopy (EIS) test results. The purpose of this work is to develop detail evaluation of the performance of this alloy in chloride-bearing environments at the interface level. The experimental results based on EIS influence the model concept, the PDM model considered a set of boundary heterogeneous reactions and transport of point defects across a passive crystalline oxide layer, the deterministic model helped to characterize the electronic properties, spatial composition distribution and the mobility properties within the layer. EIS results were used to fit the PDM and were used to determine the values of meaningful properties that can guide the path for performance of UNS S32003 in corrosive environment.

ACKNOWLEDGEMENTS

I would like to thank my advisor, Dr. Homero Castaneda-Lopez for providing the means that allowed for this project to come to completion.

I also would like to thank CERL – U.S. Department of Defense Office of Corrosion Policy and Oversight under the contract W9132T-11-C-0035 for their financial support.

My most sincere thanks to my parents, my brothers and the rest of my family for their continuous support and unconditional love.

Last but not least, I would like to thank my co-workers and group members who I also see as friends, for their continuous feedback and support and care both in and out of the lab.

TABLE OF CONTENTS

LIST OF TABLES

LIST OF FIGURES

CHAPTER I

INTRODUCTION

This chapter is dedicated to provide enough and detailed background information to understand the passive properties of a lean stainless steel alloy. The importance of the characterization of these alloys lies in the application of this material under certain corrosion environments.

1.1 Corrosion resistant alloys

The use of corrosion resistant alloys (CRA's) is one approach to overcome corrosion and risks in different industrial sectors. The range of these applications covers structural, oil and gas, automotive and different assets, been either in use or stationary conditions. Due to the aggressive nature of the environment, there is a constant threat in the reliability and performance of metallic parts in different assets and facilities. Thus, a conscious material selection is recommended for every particular application[1].

One advantage of CRA's is that there is no need for any other control action for corrosion protection, such as the use of coatings or cathodic protection, however they do involve a relatively high investment cost.

The most commonly used CRA's include commodities such as austenitic stainless steels. For applications requiring higher strength and hardness, martensitic stainless steels can be selected, unfortunately, their corrosion behavior is significantly dependent upon the heat treatment and tempering conditions which produce the optimum mechanical properties but also produce the least optimal corrosion resistance properties.

Lean duplex stainless steels can be a cost effective solution for applications in chloride containing environment; however, high chloride concentrations and temperature can set a localized corrosion risk factor that has to be addressed differently. Different lean duplex such as UNS S32003 offer a new route to overcome chlorides at different temperatures while maintaining mechanical strength. The Molybdenum-enhance alloy confers specific microstructure to the material to give a phase balance similar to a duplex stainless steel [2].

Ferritic-austenitic duplex stainless steels combine high corrosion resistance with high strength and are a good candidate to substitute standard austenitic grades in many applications. The strength might even result in reduced dimensions and thereby lighter constructions.

Another advantage of duplex stainless steels is that they use nickel instead of a high carbon alloying content in order to achieve the austenitic phase, the group of nickel-martensitic steels have a corrosion behavior which is independent of the heat treatment. The mechanical strength and hardness are as high as those of the carbon martensitic stainless steels. And they also can be easily welded.

Table 1.1 shows the mechanical properties of several corrosion resistant alloys. UNS S32003, UNS S32101 and UNS S32304 are lean duplex stainless steels, UNS S31603 is the commercial type 316L and UNS S32205 is a duplex stainless steel. Mechanical properties of a material usually dictate the application where it will be used, although this is not the only criteria as corrosion behaviour can also limit the range of application.

Table 1.1. Mechanical properties of different corrosion-resistant alloys.

	Yield, ksi	Tensile, ksi	Elongation, %
UNS S32003	65	90	30
UNS S32101	65	94	30
UNS S32304	65	110	30
UNS S31603	25	70	40
UNS S32205	65	95	25

This work will focus on UNS S32003 which as described previously is a part of the lean duplex stainless steel category of CRA's. The electrochemical nature of its corrosion resistant properties coming from the passivity of the oxides formed on the exposed surface is characterized and analyzed by using experimental approach and deterministic modeling.

1.2 Passivity and general characteristics of UNS S32003

UNS S32003 is a lean duplex stainless steel created to compete in performance against UNS S31603 (type 316L) without falling in the price range of more specialized alloys such as UNS S32205, being the former an austenitic type that is more susceptible to localized corrosion and the latter a duplex stainless steel with higher content of molybdenum and nickel. UNS S32003 is used for cable trays, ladders, flexible flow-lines, umbilical tubes and structural applications, many of these applications involve

replacing 316L parts where the environment is too aggressive, for example, at temperature ranges where pitting corrosion for this material is stable.

The Critical Pitting Temperature (CPT) for 316L is found to be about 19 ˚C when immersed into a 1.0 M NaCl solution, whereas the CPT of UNS S32003 is expected to be of about 38°C. Furthermore UNS S32003 can also be used in applications that UNS S32205 is considered as a mean to be more economically efficient as long as UNS S32003 is capable of withstanding those mechanical and corrosive conditions.

Table 1.2 shows the typical values of pitting resistance equivalent number (PREN) based on an empiric formula that depends upon the contents of chromium, molybdenum and nitrogen[3]. Table 1.3 gives the range of alloying contents of UNS S32003[4]. From values of both of these tables it can be illustrated the place that UNS S32003 stands in the industry, both the PREN and the Nickel contents dictate the value of price and performance of this alloy.

Table 1.2 Typical values of PREN for commonly used corrosion resistant alloys.

Grade	UNS	Type	PREN
430	S43000	Ferritic	18
304	S30400	Austenitic	19
441	S43932	Ferritic	19
RDN 903	S32001	Duplex	22
316	S31600	Austenitic	24
444	S44400	Ferritic	24
316L 2.5 Mo	S31603	Austenitic	26
2101 LDX	S32101	Duplex	26
2304	S32304	Duplex	26
DX2202	S32202	Duplex	27
904L	N08904	Austenitic	34
2205	S32205	Duplex	35
Zeron 100	S32760	Duplex	41
Ferrinox 225	S32550	Duplex	41
2507	S32750	Duplex	43
6% Mo	S31254	Austenitic	44

As seen in table 1.3 there is an enhancement of nitrogen into the UNS S32003. Normally nitrogen could bring fragility, however in this case the nitrogen is used to elevate the PREN as indicated in equation 1.1.

$$PREN = \% Cr + 3.3 \% Mo + 16 \% N \quad (1.1)$$

There is also the addition of Molybdenum that stabilizes the ferrite giving the microstructure the qualities of a regular duplex stainless steel. This duplex microstructure often helps remediate stress corrosion cracking problems, a quality that less advanced materials such as type 316L and are regularly forbidden for stress corrosion cracking applications. In these cases, replacing type 316L with a duplex stainless steel is highly encouraged.[5]

Table 1.3. Chemical composition of several corrosion resistant alloys[6].

	C	Mn	P	S	Si	Cr	Ni	Mo	N	Cu
UNS S32003	<0.03	<2	<0.03	<0.02	<1.0	19.5 - 22.5	3.0 - 4.0	1.5 - 2	0.14 - 0.2	0.1 - 0.60
UNS S32304	<0.02	<2	<0.03	<0.02	<1.0	22.0 - 24.0	4.5 - 5.0	0.05 - 0.60	<0.1	0.05 - 0.60
UNS S31603	<0.03	<2	<0.045	<0.03	<0.75	0.16 - 0.18	10.0 -14.0	2.0 - 3.0	<0.1	0.1 - 0.60
UNS S32205	<0.03	<2	<0.035	<0.02	<1.0	22.0 - 23.0	4.5 - 6.5	3.0 - 3.5	0.14 - 0.20	0.05 - 0.60

In many cases, stainless steels that form passive films have properties that are dependent upon the applied potential; passive films that are created at low potentials may be rich in chrome oxides whereas the films created at higher potentials may be formed mainly by iron oxide due to the reaction kinetics[7]. In the case of lean duplex stainless steels, the addition of molybdenum enhances the passive layer according to several theories increases its stability[4]. From the contents of the alloy two types of layers are typically formed on the surface of the metal. A chromium rich oxide layer which will act as a barrier/protective layer and after a porous diffusive iron rich layer,

which despite of its permeability, it will add to the ohmic drop when accounting for interfacial reactions at each sides of the layers.

UNS S32003 has a dual phase microstructure of austenite and ferrite, the combination of these phases allow this material to achieve elevated levels of mechanical properties, such as yield strength, which is 517 MPa in the case of UNS S32003 which is significant compared to that of a type 316 which only has 276 MPa[8]. For the S32203 each of its molybdenum stabilized phases will retain different contents of alloying elements that can result in a dual type passive layer. Thus, the electronic properties are expected to be dual in nature. No real surface must be considered perfectly homogeneous, the existence of surface roughness, impurities, dislocations, grain boundaries, distribution of active sites, predominance of cation and/or anion vacancies and interstitial prevent the idealization of an electrical analogue, hence the reason of the fabrication of a model that is focused on the defects based on experimental measurements.

1.3 Point Defect Model

From a deterministic point of view, breakdown of the passive layer occurs due to the transport of defects from the surface of the oxide to the metal/metal oxide interface. A viable way to study the behaviour of a metal/metal oxide is to create a Point Defect Model (PDM) [9] at every specific condition, to recreate the response of EIS tests [10]. Many PDM's have been created to simulate different parts of the electrochemical and microstructural process, care should be taken when considering the most significant aspects and further inspection and characterization of the passive layer is required using, for example, X-Ray Photoelectron Spectroscopy (XPS) studies of depth

chemical analysis. Furthermore, using a Mott-Schottky analysis will determine the type of semiconductor behaviour the layer is adopting. This is particularly useful when constructing the PDM to determine the dominant defect that is participating in terms of charge carrier [11]. It is generally accepted that there is a correlation between the crystallographic defect structure and the electronic structure of the passive film. For type n semiconductors the predominant crystallographic defect in the barrier layer is the oxygen vacancies and/or anions and cations interstitials, and for the p-type semiconductors the majority of the defects are cation vacancies acting as acceptors. Each or these behaviours can determine which interfacial reaction or reactions are most important for the contribution of passivity breakdown.

Different conceptual point defect models have been proposed. The first original Point Defect Model was developed by Chao, Lin and Macdonald[12] explaining the growth and breakdown characteristics of passive films. The point defect model was used to interpret the anodic behaviour of oxide films on iron and nickel which was later referred to as “first generation PDM”. This model allowed describing the impedance spectra and evaluating small effects of alloying elements and solutions containing aggressive anions such as chlorides.

The second generation came when other assumptions such as breakdown voltage and induction time parameters were taken into account, which restricted the experimental data to assuming steady-state (or quasi-steady-state) conditions. The third generation PDM was recognized as the ones who were able to estimate oxide layer thickness and completely balanced out a set of point defect reactions. The more common reactions that are considered for modern all-inclusive PDM are shown in figure 1.1.

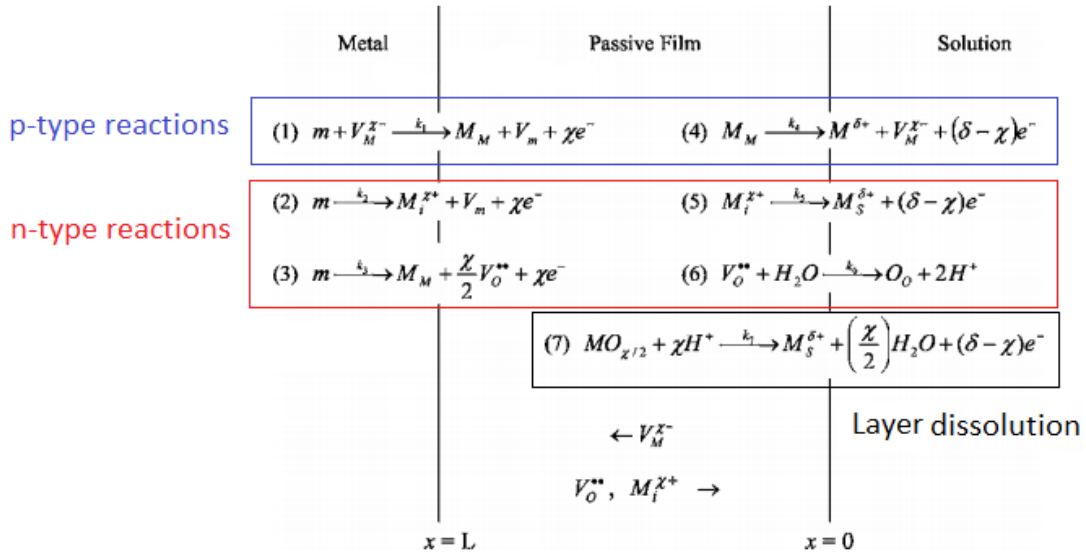

Figure 1.1. All-inclusive set of reactions available based on point defects across a passive oxide layer.

One of the biggest obstacles when working with a point defect model is the validation of the preponderant defect that would be responsible to control the process as the limiting step.

Other useful electrochemical techniques can be used as indicators of interfacial reactions that are related to a current density [7], such are the reactions proposed in figure 1.1 with the exception of reaction 6. By applying potentiostatic polarization (PP) at potentials where the material is passive, a steady state current can be evaluated. Cyclic Potentiodynamic Polarization (CPP) is used to detect the potential zones where the material is passive and susceptibility to localized corrosion if localized corrosion starts.

In this work, the study of the passivation of UNS S32003 has been performed by means of XPS and Electrochemical techniques such as Cyclic Potentiodynamic

Polarization (CPP), Potentiostatic Polarization (PP), Mott-Schottky Analysis and Electrochemical Impedance Spectroscopy (EIS). The experimental findings are used as the basis for proposing a PDM, which predicts the behaviour of the metal and evaluate its performance in each of the experimental conditions studied.

CHAPTER II

EXPERIMENTAL DESIGN

This chapter will cover in general the experimental set up that was carried out in order to study the interfacial anodic behaviour of UNS S32003 in chloride media. Commercial brands of equipment and material may be mentioned once and then referred by their generic name of the item. More specific details about the experimental set up may be given in their corresponding sections.

2.1 UNS S32003 Sample preparation

UNS S32003 samples for electrochemical tests were ground with SiC sand paper until 600 CAMI grit designation. For XPS Analysis the samples were ground until 1200 to prevent the interference of the surface roughness in the passive film analysis. Each specimen was degreased with ethanol and rinsed with copious amounts of distilled water. After grinding the specimens were put to clean ultrasonically.

2.2 Electrochemical techniques

Electrochemical experiments were carried out in a three-electrode arrangement in an Avesta Cell to prevent crevice corrosion. All electrochemical experiments were performed using a Solartron 1287 Electrochemical Interface and a Solartron 1260 Frequency response analyzer. A heating mantle was installed on the cell to control the temperature.

The working electrode consisted of 2-inch-squared plates of UNS S32003 Lean Duplex Stainless Steel with a circular area of 5 cm^2 exposed to the solution. The reference electrode used on all tests was a silver/silver chloride electrode (Ag/AgCl; 0.235 V vs SHE) designed for high temperatures and the counter electrode was a platinum mesh placed parallel to the working electrode to achieve a better current distribution. For all electrochemical test experiments, the electrolyte was a deaerated 1 M, 0.5 M, or 0.1 M NaCl solution at room temperature.

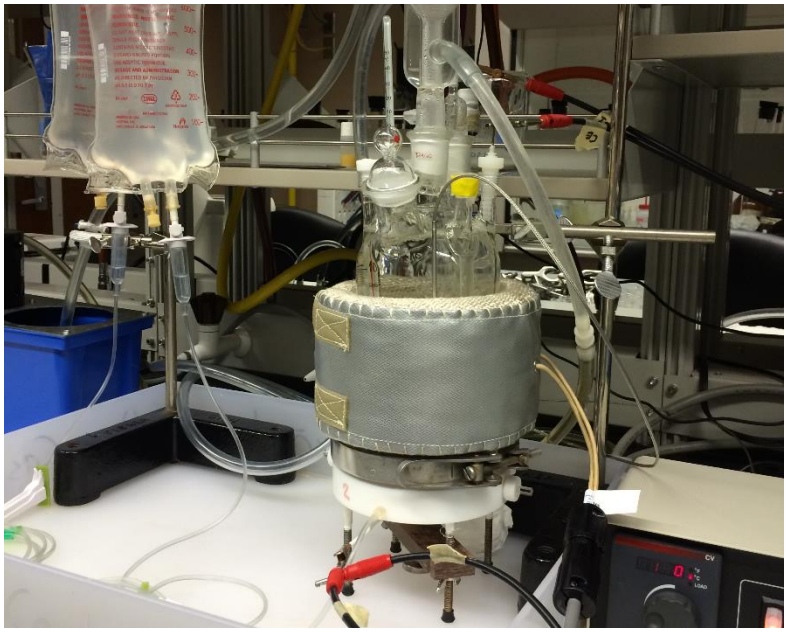

Figure 2.1. Electrochemical cell and attachments used.

2.3 Direct current electrochemical techniques

Direct current (DC) electrochemical techniques were used as accelerated tests to study the unsteady-state behaviour of the alloy, these include cyclic potentiodynamic polarization (CPP) and potentiodynamic polarization (PP).

2.3.1 Cyclic potentiodynamic polarization

CPPs were performed for UNS S32003 for every concentration; a steady-state period of 1 hour of open circuit potential was monitored before polarizing the specimen. For CPPs, the potential scan rate was 1 mV/s and 200 mA/cm^2 was the indicator for scan reversal. All specimens were analyzed with a stereoscopic microscope at a magnification of 50x to optically evaluate if pitting corrosion occurred. CPP was performed by following the standard protocol for the ASTM G-61 test [13].

2.3.2 Potentiostatic polarization

From the polarization curves, different potentials in the passivity zone of the materials are selected to run potentiostatic tests. The specimen was polarized to a selected potential within the passive region and get an steady state current density (in the order of 10^{-5} A), thus allowing the use of EIS as mean to characterize the nature and phenomena occurring at the interface, the potentiodynamic polarization process took 12 hours in average for all tests. Potentiostatic polarization was also performed according to the standard protocol for the ASTM G-150 test for analysing Critical Pitting Temperature (CPT) [14].

2.4 Alternating current electrochemical techniques

Alternating current (AC) electrochemical techniques were used to study the steady state behaviour of the alloy, these include electrochemical impedance spectroscopy (EIS) and Mott-Schottky AC potential sweep.

2.4.1 Electrochemical impedance spectroscopy

EIS was measured after 12 hours of PP. The frequency range used was between 0.01 Hz and 100 kHz with an amplitude of 10 mV, the EIS test was performed in both scan directions to reveal the validity of the data with regard to the stability constraint.

2.4.2 Mott-Schottky AC potential sweep

Mott-Schottky Analysis was also performed following 12 hours of polarization, a constant frequency of 1000 Hz was used to bring back the sample from the 0.8 V to -0.1 V vs Ag/AgCl at a rate of 10 mV/s, which is high enough rate to detect the electronic properties of the semiconductor that was being tested. The effect of the environment on the electronic properties of the passive layer was evaluated for 1.0 M, 0.5 M, 0.1 M, and 0.01 M NaCl solution.

2.5 X-ray photo electron microscopy

XPS analysis was performed on three electrochemically tested samples to measure the effect of the applied potential over the composition of the passive layer formed. The concentration at which they were tested was 0.5 M for the polarization of 0.2 V, 0.5 V and 0.8V vs Ag/AgCl. The samples were sputtered to measure the elemental concentration of every species of interest against the depth of the layer, the argon-ion gun used an energy of 3.0 kV over a 5.0 x 5.0 microns area and was calibrated to measure about 7.2 nm for every minute of sputtering.

2.6 Surface Analysis Techniques

Optical microscopy and scanning electron microscopy (SEM) were used to evaluate the damage effects of the pitting events that occurred on the sample surface in some of

the electrochemical tests. By using a macro scale with the optical profilometer, the pit depth was estimated, which helps in evaluating the extent of the damage. In addition, SEM can identify the different surface features that resulted from the attack on the microstructure, which is helpful to postulate a mechanistic approach that considers the spatial distribution of a dual-phase microstructure.

CHAPTER III

EFFECT OF TEMPERATURE

This chapter focuses on the effects of temperature on UNS S32003, using type 316L as a control.

3.1 CPP at different temperatures

Figure 3.1 A shows the response, in current, of UNS S32003 to the applied potential; at temperatures of 40˚C and above, the potentiodynamic curve showed a small passive region and a positive hysteresis, indicating that pitting corrosion always occurred at these temperatures. Below 40˚C, the potentiodynamic curve showed a much larger passive region and negative hysteresis, indicating that pitting corrosion was unlikely to occur. This behavior did not appear in the potentiodynamic curve for 316L at any temperature (Figure 3.1 B). For all the temperatures tested, the passive region was very small and transpassivity occurred at the same potential, which can be attributed to the oxygen evolution reaction [15], and the curve always showed a positive hysteresis. The 1M NaCl solution is such an aggressive environment for 316L that 316L's CPT was below 25°C, indicating that this material was more susceptible to pitting corrosion than UNS S32003 at room temperature.

3.2 ASTM G-150 test for CPT

Figure 3.2 shows the results of the ASTM G 150 test. As shown in the polarization plots, breakdown occurred between 35 and 40^{0}C at about 0.9 V vs Ag/AgCl; to ensure breakdown and obtain a CPT independent of potential, 1.0V vs Ag/AgCl was selected, which is higher than the potential recommended from the standard, to increase the reliability of the results (700 mV vs SCE, which is about 658 mV vs Ag/AgCl). 100 μA/cm^2 were reached at about 36.7^{0}C, which is consistent with previous experiments [16].

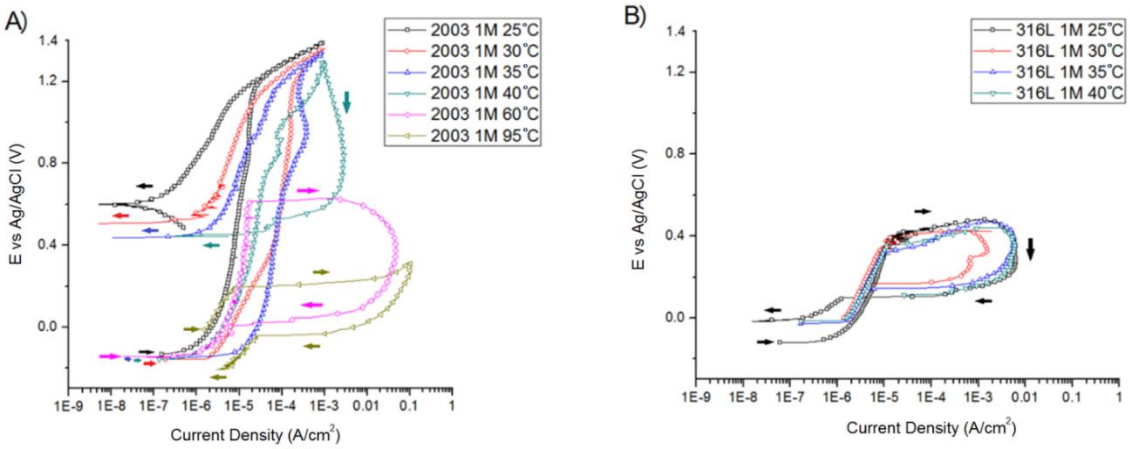

Figure 3.1. Cyclic Potentiodynamic Polarization plots at different temperatures A) UNS S32003 Lean Duplex Stainless Steel, B) 316L Austenitic Stainless Steel.

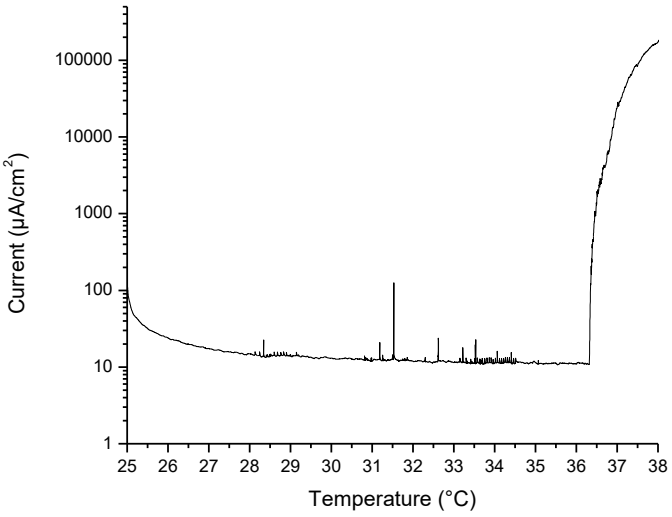

Figure 3.2. ASTM G 150 test on UNS S32003.

3.3 Optical inspection

Figure 3.3 shows the micrographs of the surface of UNS S32003 following the CPP tests where pitting corrosion occurred. The pit density increased proportionally with increased temperature; this behavior is similar to the results for 316L, as shown in Figure 3.4, where pitting corrosion was stable at 25^0C. Figures 3.5 and 3.6 show the infinite focus microscope results where the depth of an individual pit could be quantified and the morphology and physical aspects of the pits can be observed. The average pit depths of every sample are reported in Table 3.1. No statistical analysis was needed since the changes in depth were not significantly different under different conditions. For example, UNS S32003 had 120 μm -deep pits from 60 to 95˚C and localized attack was not evident at these temperatures; at 40˚C, the pits were 70 μm deep. This same trend repeated with 316L: at 30 ˚C, the depth of the pits were about 45 μm, but at 40˚C, where UNS S32003 was starting to have pitting corrosion, the pit depth for 316L was already about 145 μm, deeper than UNS S32003 at 90˚C.

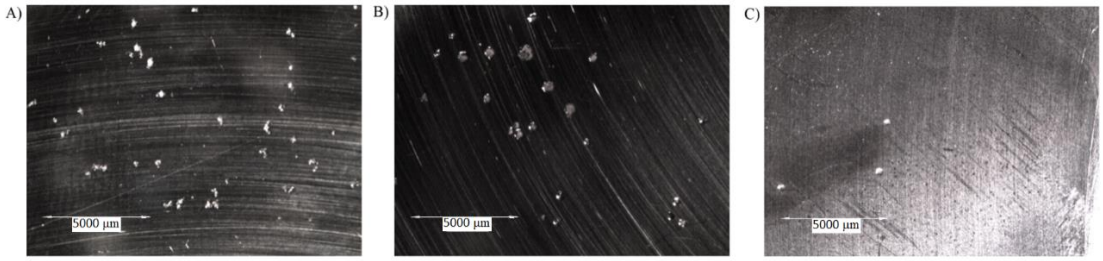

Figure 3.3. Surface of UNS S32003 samples at different temperatures after CPT. A) 95˚C, B) 60 ˚C, C) 40 ˚C.

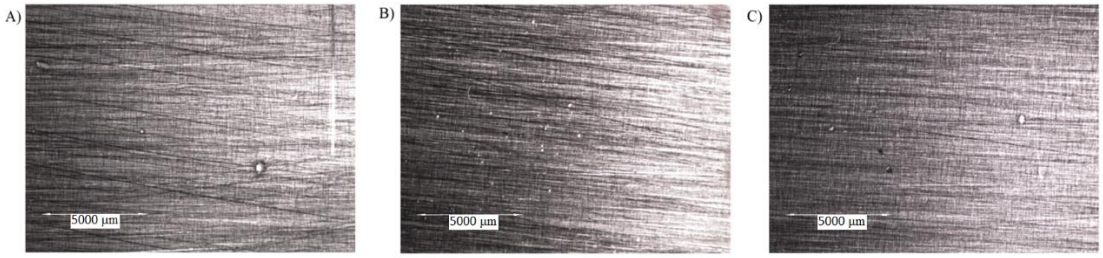

Figure 3.4. Surface of 316L samples at different temperatures CPT. A) 40˚C, B) 30 ˚C, C) 25˚C.

3.4 EIS analysis with electrical analogues

UNS S32003's EIS response was obtained at 35 ˚C at different potentials within the passive region that was previously defined by polarization techniques. These conditions were selected because of the interest in studying the phenomena and processes that occur when the metal is passive at the more critical conditions before pitting corrosion begins; EIS is not used for localized corrosion, such as pitting corrosion, due to the stability principle needed to apply the EIS technique.

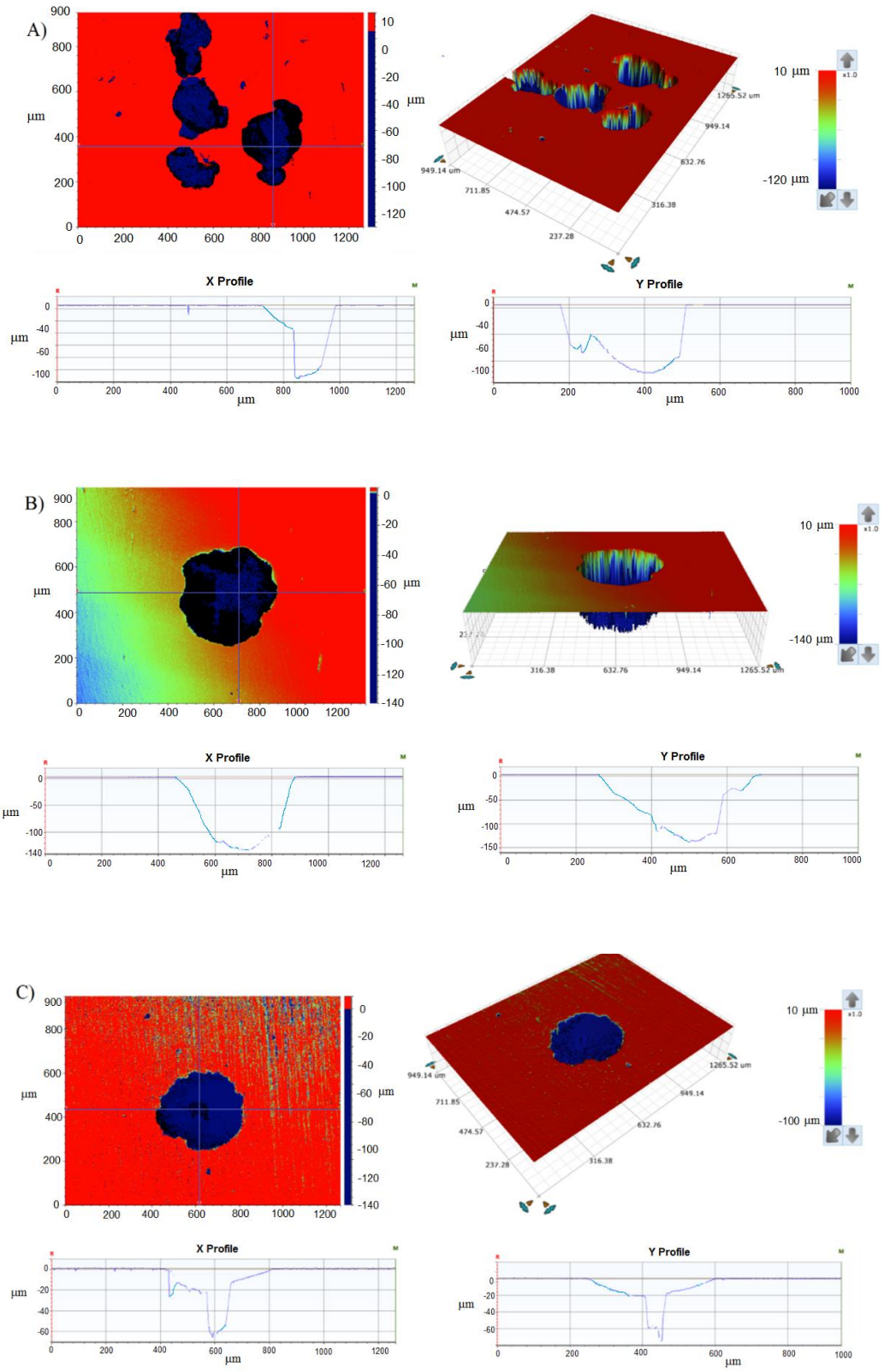

Figure 3.5. Surface Analysis of average pit at different temperatures after CPP on UNS S32003. A) 95˚C, B) 60 ˚C, C) 40 ˚C.

The potentials that were selected for EIS testing at potentiostatic conditions were: the transition from active to passive (0.2 V), within the passive region (0.5 V and 0.8 V), and close to the transpassive zone (1 V). The response of EIS was also measured on 316L but only at 0.2 V, where a steady-state could be achieved; above this potential, there is no more passive region under the experimental conditions and performing EIS does not provide relevant information [17]. Figures 3.7(A,B) and 3.8(A-D) show the fitting on the impedance data in Nyquist, Bode, and phase angle representations; different models could be used to fit these data, but the selected models reveal the physical meaning of the process, using the variables of faradaic resistance (R_f), double layer capacitance (CPE), pore resistance (R_p), and pore capacitance (C_p). The model can also be applied to 316L when applying a potential of 0.2V because of the protection by the same bi-layer mechanism; however, the range of potential where it is possible to reach the steady-state formation of a passive layer is smaller in 316L than in UNS S32003, because short increments in potential (higher than about 0.2 V) would force the 316L sample to go above its repassivation potential, where the appearance of meta-stable pits increases. Additionally, extended periods of polarization generate stable pitting corrosion, and therefore the EIS results cannot be interpreted because these issues make steady-state conditions impossible [18].

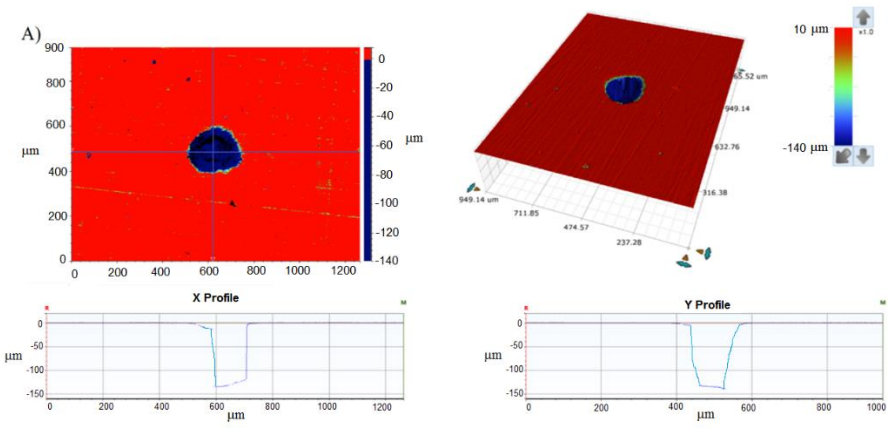

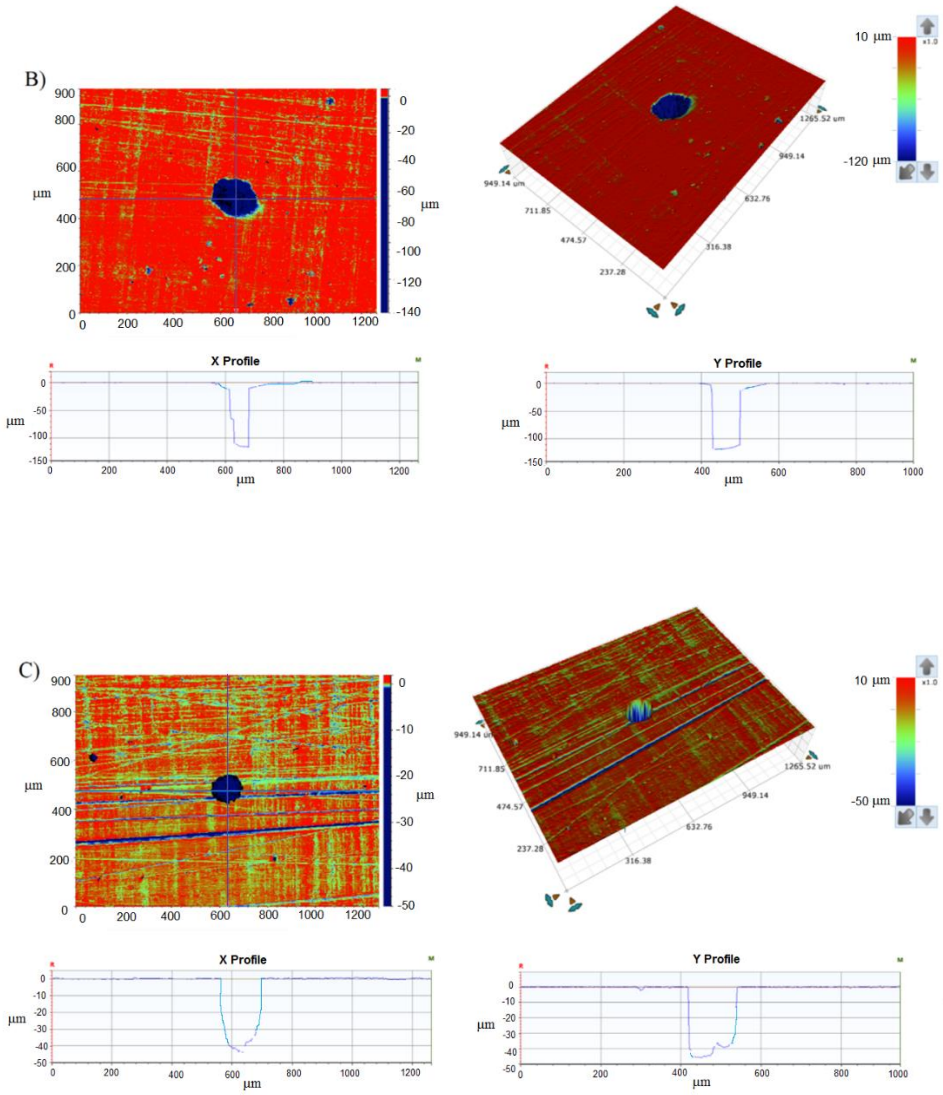

Figure 3.6. Surface Analysis of average pit at different temperatures after CPP on 316L. A) 40˚C, B) 30 ˚C, C) 25 ˚C.

Table 3.1. Average depth of pit for UNS S32003 and 316L at different temperatures.

	95 ^{0}C	60 ^{0}C	40 ^{0}C	35 ^{0}C	30 ^{0}C
UNS S32003	120 µm	125 µm	75 µm	-	-
316L	-	-	145 µm	125 µm	45 µm

As shown in the following chapter, the passivation of a metal occurs from the formation of two layers [19], a thin *inner* protective barrier layer that is formed on the metal surface, which in the case of stainless steel is made mostly of chromium oxide, and a diffusive outer layer that can be rich in iron oxide and other elements; this second layer is porous and the electrolyte can diffuse through it, though when it reaches the barrier layer only the oxygen will react by occupying oxygen vacancies in the Cr_2O_3 structure. Therefore, there will be diffusion of species within the porous layer and only diffusion of oxygen vacancies through the barrier chromium oxide layer, and these reactions will occur at the interface of the oxide layers. The behavior of these two layers in contact with the electrolyte can be represented by an equivalent circuit analogue, shown in Figure 3.9. In this electric analogue, *Cp* and R_{pore} represent the capacitance and electric resistance, respectively, of the diffusive, porous outer layer and *CPE* and *Rf* are related to the faradaic reversible process occurring at the interface between the oxide layers; *CPE* represents a pseudo-capacitor, which will correlate to an effective capacitance of an electrochemical double layer utilizing the Brug's equation [20]:

$$C_{eff} = Q^{\frac{1}{\alpha}}(R_{pore}^{-1} + R_f^{-1})^{(1-\alpha)/\alpha} \quad \text{.....(3.1)}$$

Equation 3.1 indicates that for the specific circuit, an effective capacitance will depend on the electric resistances described above and also to a parameter *Q* and an exponent α, which will be obtained by the fitting of the curve.

In Table 3.2, the electrical elements according to the selected model are shown; C_{eff} values are in the range of capacitance of an electrochemical double layer, which supports the selected equivalent circuit. The values of *Rf* increase proportionally with

the applied potential and only decrease at the highest polarization due to the transpassive behavior, suggesting that the alteration of the faradaic process may not affect the rate of reaction; this may be an indication of the transport of oxygen vacancies through the barrier chromium oxide layer. The capacitance of pores decreases by two orders of magnitude, from 0.8 V to 1 V vs Ag/AgCl; this change from capacitive to resistive behavior could indicate a more permeable layer, i.e., that the transport of the charge species is more favorable, which is possible considering that the contents of iron oxides at the diffusive passive layer formed at such a high potential have increased. Consequently, as the content of iron oxides increase, the more porous the diffusive layer will be, although further surface analyses, such as XPS and SEM analyses, are recommended to support this hypothesis.

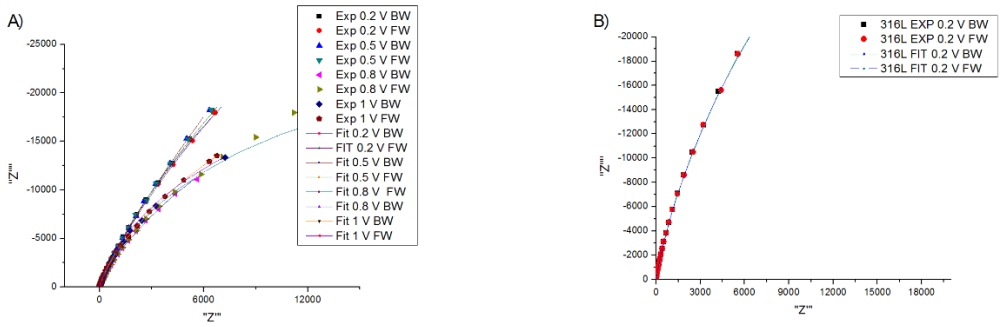

Figure 3.7. Nyquist plots with calculated fitting to the proposed model. A) For UNS S32003 Lean Duplex Stainless Steel, B) 316L Austenitic Stainless Steel.

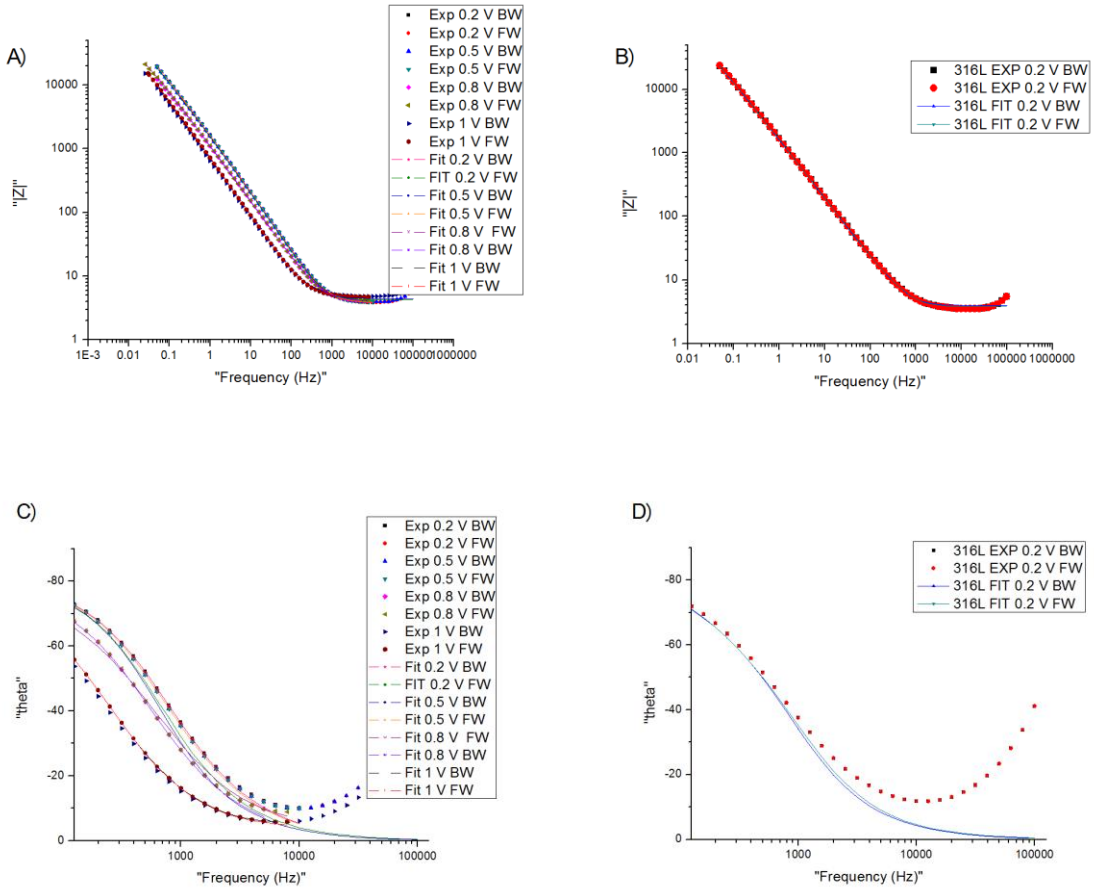

Figure 3.8. Bode plot for A) for UNS S32003 Lean Duplex Stainless Steel, B) 316L Austenitic Stainless Steel. And Phase angle plot for C) for UNS S32003 Lean Duplex Stainless Steel, D) 316L Austenitic Stainless Steel.

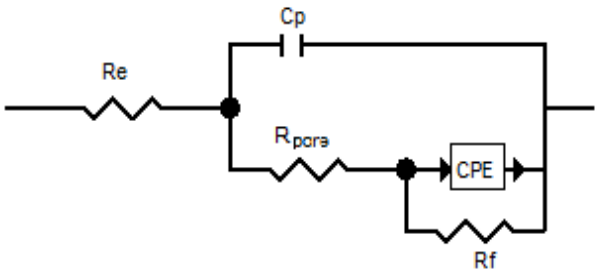

Figure 3.9. Equivalent circuit proposed to characterize and analyse impedance data.

Table 3.2. Parameters calculated at different potentials according to the equivalent circuit proposed.

Alloy	E vs Ag/AgCl (V)	C_p ($F*cm^{-2}$)	Rpore (ohm/cm^2)	CPE-T ($F*cm^{-2}s^{-\alpha}$)	CPE-P (α)	R_f (ohm/cm^2)	C_{eff} ($F*cm^{-2}$)
2003	2.0E-01	4.2E-05	5.3E-01	9.5E-05	7.8E-01	1.6E+05	7.2E-06
	5.0E-01	4.6E-05	7.2E+00	8.6E-05	7.6E-01	2.6E+05	8.0E-06
	8.0E-01	4.6E-05	1.9E+00	0.0001454	7.9E-01	6.6E+04	1.7E-05
	1.0E+00	9.0E-07	1.3E+00	3.0E-04	9.0E-01	4.1E+04	1.3E-04
316L	2.0E-01	5.5E-05	2.9E+01	6.5E-05	8.1E-01	1.6E+05	1.5E-05

It can be argued that the interfacial reactions, i.e., the faradaic process that is taking place at the oxide layers, are being controlled by the rate at which point defects are being transported to the interface of the two oxide layers. Oxygen vacancies, cation vacancies, and cation interstitials are formed during the formation of the passive layer, as shown in Figure 1.1. Both oxygen vacancies and metallic interstitials are being formed at the metal/barrier layer interface, whereas cation vacancies are formed at the barrier layer/outer layer interface; these will be heterogeneous reactions that will serve as boundary conditions for a PDM. The sites that are created will go from higher to lower concentrations, meaning the oxygen vacancies and metallic interstitials that are formed at the metal/barrier layer interface will tend to be transported to the barrier layer/outer layer interface; the same will happen with cation vacancies but in the opposite direction. The transport of these defects implies carrying charge, which is an electrochemical process that contributes to the response to EIS. The diffusion of point defects may play an important role, which can be characterized by the fitting process following the EIS response. In the event that the vacancy transport is the controlling element of the process, a diffusion control type of impedance would have appeared as a noticeable Warburg element; since this is not the case in the presented conditions, a more dominant charge transfer control is assumed.

3.5 Summary of the chapter

The characterization of the electrochemical behavior of UNS S32003 and UNS S31603 at different temperatures in a 1M NaCl environment was performed by means of DC and AC techniques. Microscopy techniques were also used to characterize and provide supporting evidence of the corrosion products and passive layers formed. The equivalent circuits were used for simulating the electrochemical behavior of the interface metal/passive layer/electrolyte to reproduce the experimental data and explain the surface oxidation reactions.

The CPT for UNS S32003 is in the range of 36 to 40^{0}C, which is higher than that of 316L; therefore, UNS S32003 is a better material to use at these temperatures in corrosive solution.

The process of passivation, after reaching steady-state-like currents, was still controlled by charge transfer for both alloys, although the passivation behavior and mechanisms are expected to be different.

The following proposed model offers a good representation for the experimental results and the parameters can quantitatively represent the physical meaning of the interface.

A passive bilayer comprising a chromium-rich inner layer and an iron-rich outer layer is proposed to be formed on the interface of UNS S32003 and the electrolyte.

CHAPTER IV

X-RAY PHOTOELECTRON SPECTROSCOPY ANALYSIS ON PASSIVATED UNS S32003

This chapter includes the XPS characterization and analysis of UNS S32003. In many cases, stainless steels that form passive films have properties that are potential-dependent; passive films that are formed at low potentials may be rich in chrome oxides, whereas the films formed at higher potentials may include iron oxide due to reaction kinetics. For lean duplex stainless steel, the addition of molybdenum, according to several theories, enhances the corrosion properties and stabilizes the passive layer. From the contents of the alloy, two types of layers are typically formed on the surface of the metal: the inner, chromium-rich oxide layer, which will act as a barrier/protective layer, followed by a porous, diffusive, iron-rich outer layer, which, despite its permeability, will introduce an ohmic drop when accounting for interfacial reactions at each side of the layers.

4.1 Effect of potential on the passivity of UNS S32003

The effect of the applied potential was evaluated in this work at a constant electrolyte concentration. Figure 4.1 shows the results of the atomic percentage of each species as a function of depth, where the region where oxygen is higher represents the oxide layer. The

sputtering time can be transformed to depth, as studied by Baer et al. [21], because Fe_2O_3 is 60% and for Cr_2O_3 is 50% if one is sputtering pure SiO_2, according to the calibration of the equipment. The depth in nm is similar to the sputtering time in minutes; however, considering the appearance of different oxides, as shown in the XPS analysis, no direct relationship can be confirmed. The chromium oxide layer, which is responsible for the protection of the metal, is about 15 layers of atoms deep according to [21] for most stainless steels, corresponding to about 2 nm [22], which is consistent with the results shown in the atomic profiles. Following the path of the chromium concentration, it is noticeable that there is a maximum of a few nanometers into the passive layer; this maximum is related to the barrier layer, while the rest of the passive layer can be considered a mixture of iron oxides. Figure 4.1 A shows an unusual amount of iron in the outermost part of the passive layer and an overall bigger zone of oxides; considering that the previous electrochemical testing was at 0.8 V, it could be attributed to the high applied potential. The second layer had a considerable growth of iron-rich oxides, in contrast to that of other treatments, as seen in Figure 4.1 B and 1C.

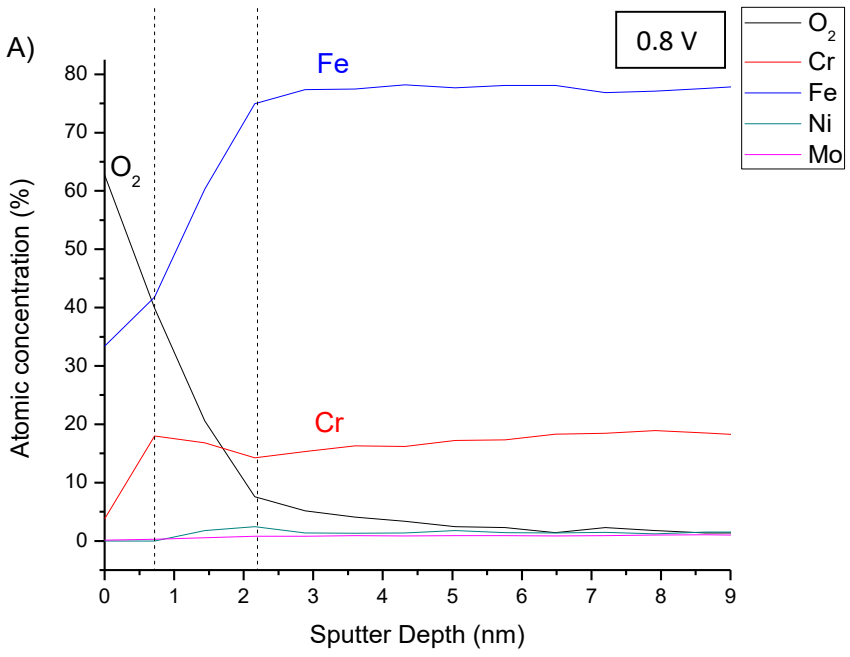

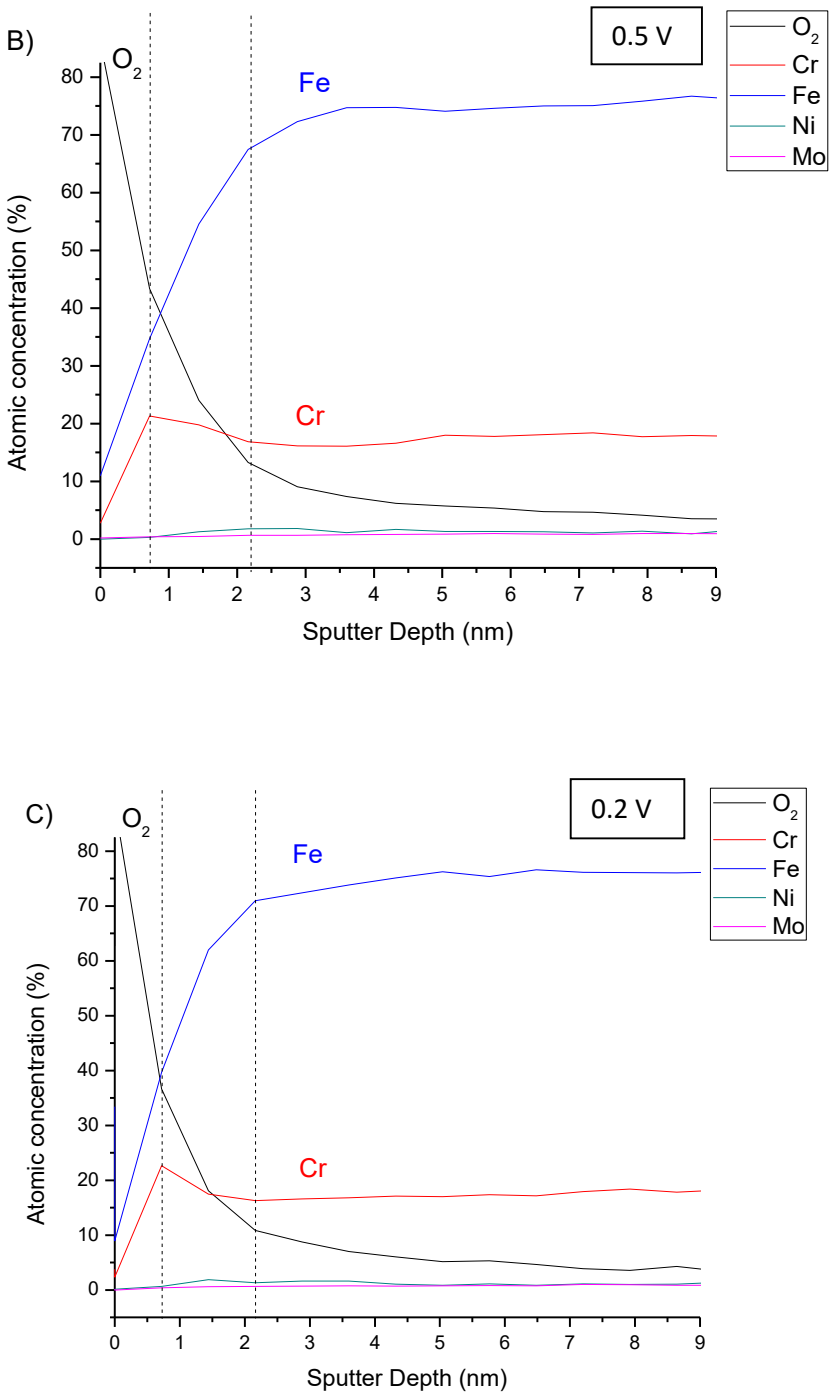

Figure 4.1. XPS analysis results showing atomic percent vs depth for the passive layer formed in 0.5 M NaCl at A) 0.8 V, B) 0.5 V and C) 0.2 V vs Ag/AgCl.

A)

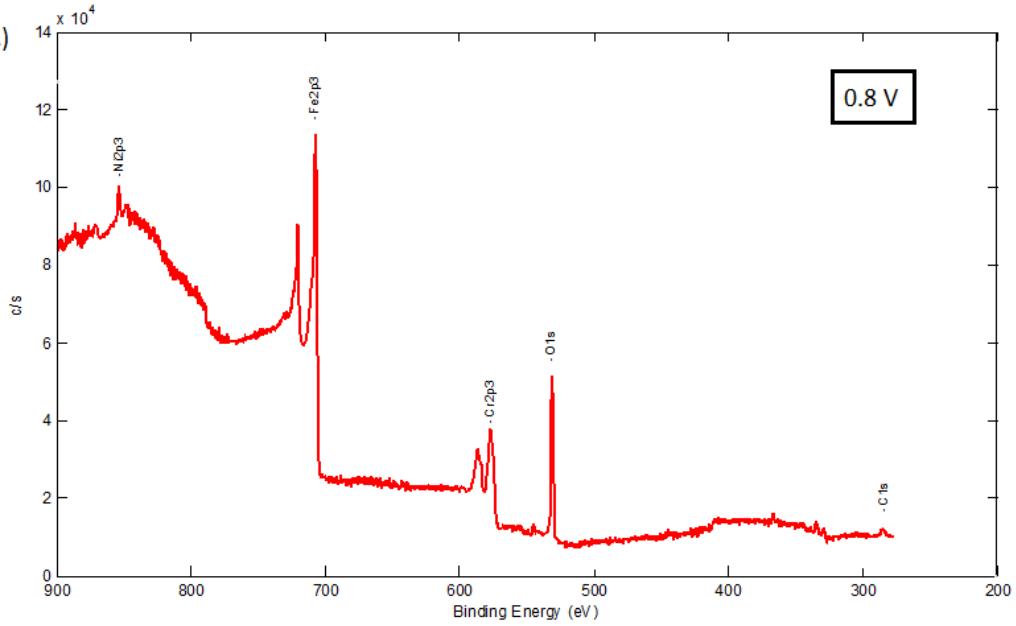
x 10^4
14
12
10
8
6
4
2
0
c/s
0.8 V
N2p3
Fe2p3
Cr2p3
O1s
C1s
900
800
700
600
500
400
300
200
Binding Energy (eV)

B)

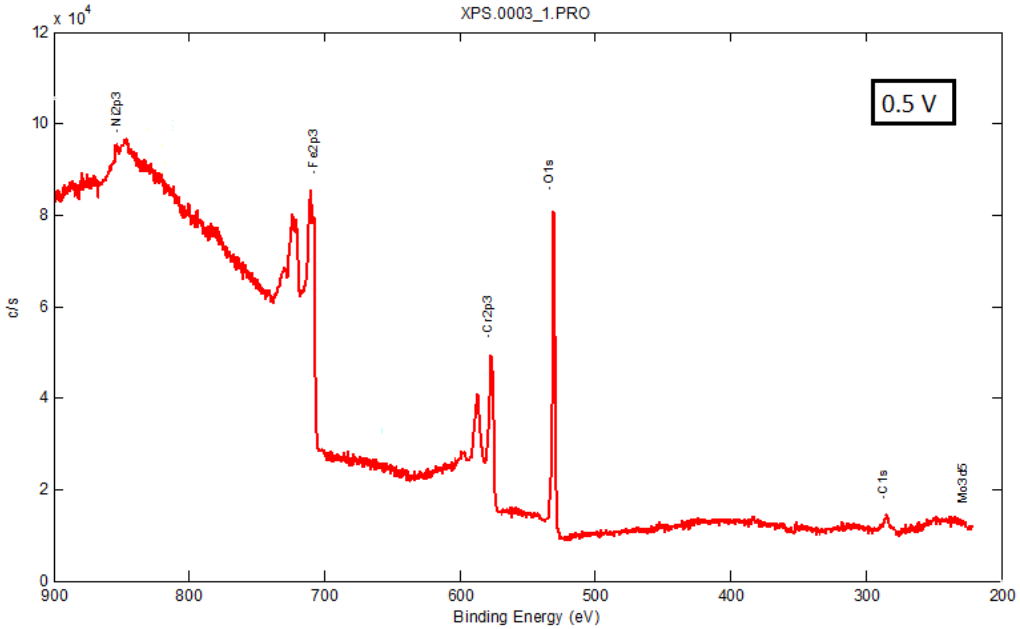
XPS.0003_1.PRO
x 10^4
12
10
8
6
4
2
0
c/s
0.5 V
N2p3
Fe2p3
O1s
Cr2p3
C1s
Mo3d5
900
800
700
600
500
400
300
200
Binding Energy (eV)

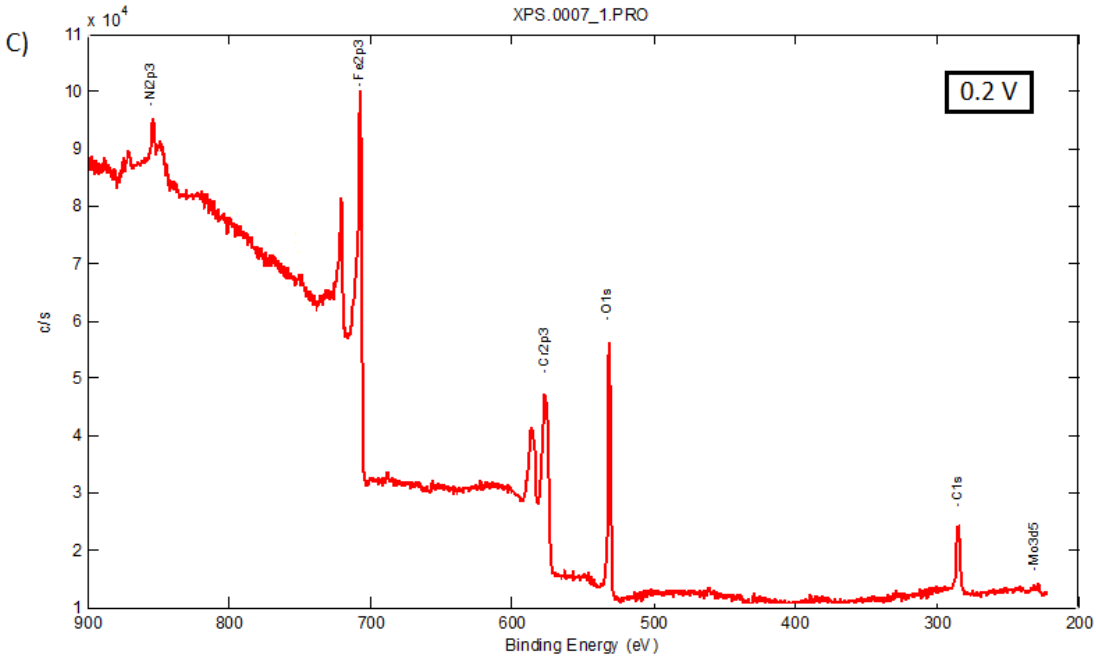

Figure 4.2. XPS results showing the outermost surface layer survey spectrum when formed in 0.5 M NaCl at A) 0.8 V, B) 0.5 V, and C) 0.2 V vs Ag/AgCl.

Figure 4.2 shows the survey scans on the original surface; these scans can be useful for quantitative comparison of the outermost components of the oxide layer formed on the samples. As previously seen, the passive layer formed on the sample that was polarized at 0.8 V vs Ag/AgCl had higher iron content (Figure 4.2 A). The sample that was polarized at 0.2 V vs Ag/AgCl had the least enrichment of iron, and the sample that was polarized at 0.5 V vs Ag/AgCl had similar results as the sample polarized at 0.2 V vs Ag/AgCl (Figure 4.2 B and C). This behavior can be related to the polarization curves shown in chapters three and five (for example, Figure 5.1), where there is defined passive region for the cyclic polarization of UNS S32003. Within this passive region, three clear zones can be distinguished: at 0.2 V vs Ag/AgCl, following the active to passive transition; 0.8 V vs Ag/AgCl, close to the transpassivity potential; and 0.5V, between the other two magnitudes. In the vicinity of 0.8 V, a “hump” or a “second passivation” occurs and the current density decreases before entering the zone where

oxygen evolution occurs. This drop in current is likely to be caused by the rapid appearance of a second protecting agent, which is believed to be the ohmic drop caused by the growth of the outer layer. This can also be seen in the XPS results at 0.8V of pretreatment, indicating that at 0.8 V vs Ag/AgCl, the iron oxide formation reaction is much faster in such a way that an ohmic drop is caused within its porous geometry, causing the decrease in current. It should be noted that the iron oxide formation reaction is occurring at all times; however, at 0.8 V vs Ag/AgCl, the reaction is much faster.

4.2 UNS S32003 bi-layer system of oxides

The growth of a the second layer, mostly comprised of oxides and hydro-oxides of iron, has been found and reported elsewhere [19] where the times of exposure were considerably longer than in this work. The assumption of a dynamic system of layers can lead to deviations when assessing the protective behavior of a passive metal; even if the iron-rich layer is permeable and not being considered as the rate-limiting step, the ohmic drop formed by it must be considered.

It is interesting to note that the contribution of a thicker iron-rich oxide layer could be beneficial to the corrosion properties of the alloy due to the generated ohmic drop. The results from the accelerated tests have been presented; however, in field conditions, anodic polarization is not applied to these alloys that can pass the energetic barrier of the iron oxide formation reaction, meaning that this layer will form slowly and over extended periods of time. It is important to notice that the chromium oxide barrier layer is acting as an inner layer, which implies that there will also be a physical barrier that will obstruct the movement of iron species to the outer surface; this type of transport can be explained by considering that the atomic size of iron is similar to that of the

chromium, allowing it to take its place in the hexagonal structure of the chromium oxide structure, filling in cation vacancies that are preponderant for this acceptor-type of oxide. Therefore, iron species can move through the porous outer layer, where oxygen should be readily available for the iron species to react, thus growing the outer iron oxide layer, i.e., the acceleration at 0.8 V vs Ag/AgCl does not affect the kinetics of iron oxide formation but accelerates the cation vacancy generation on the chromium oxide barrier, consequently increasing the availability of iron ions in the barrier layer/oxide layer interface.

4.3 Summary of the chapter

A chromium-containing oxide layer of approximately 6 nm was found adjacent to the substrate and is considered responsible for the passivity and protection of the metal.

An inner chromium-rich oxide layer and an outer iron-rich oxide layer were formed in all cases. The thickness of the outer layer was similar in the 0.2 V and 0.5 V vs Ag/AgCl treatments, which were smaller than that of the sample prepared at 0.8 V vs Ag/AgCl.

Correlations between the typical cation vacancies for a chromium-rich oxide layer and the formation of the outer layer can be found; thus suggesting an explanation for the growth of the bi-layer system.

CHAPTER V

SEMICONDUCTING PROPERTIES AND PDM PROPOSAL

In this chapter, the semiconducting nature, preponderant defects, and charge carriers, defined by Mott-Schottky analysis, of UNS S32003 are presented. When incorporating the previous chapters with the information obtained from AC electrochemical techniques, a PDM is proposed and optimized to the EIS spectra.

5.1 DC electrochemical techniques

CPP was performed to identify the passivity region of UNS S32003 and evaluate the effects of NaCl concentration on its direct current (DC) properties.

The effect of the Cl^- is especially of interest as it is often considered responsible for passivity breakdown [23]. Figure 5.1 shows the CPP curves of UNS S32003 at different chloride concentrations. There is no positive hysteresis in these CPP curves, which assures that no localized corrosion is stable at these conditions. Other authors [24] [25] have found metastable pits on the ferrite phase in stainless steel in a chloride-containing environment, suggesting that it is natural to expect current transients when applying a potential on the alloy due to the formation and repassivation of metastable pits. In this case, current transients appeared sporadically, although they are worth mentioning.

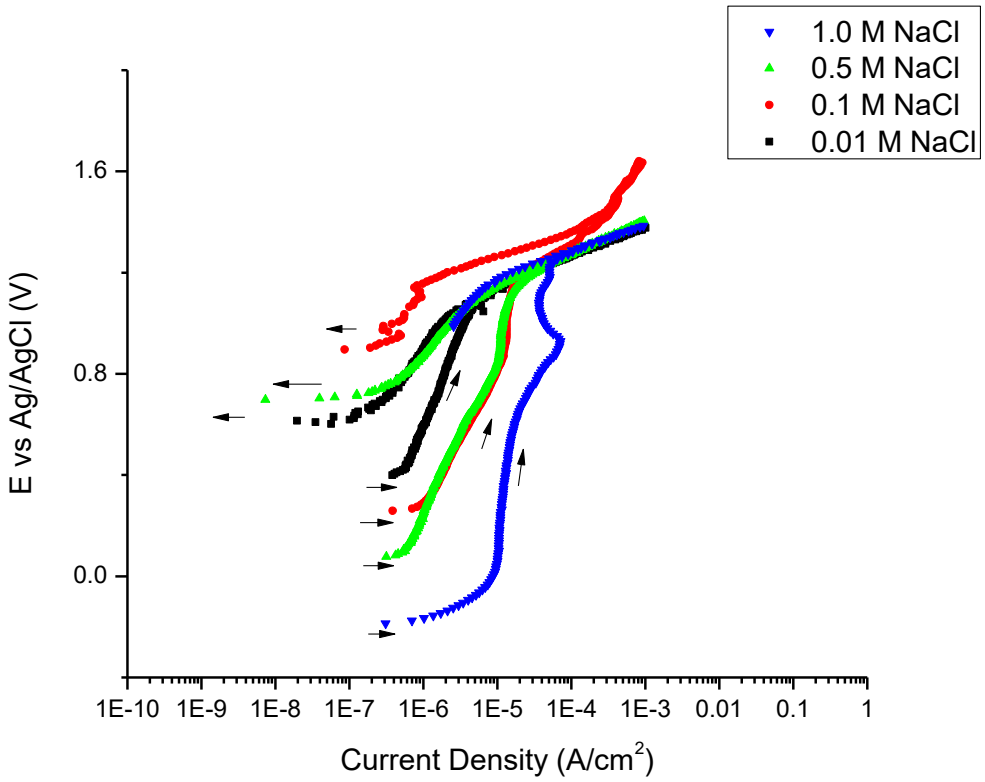

Figure 5.1. CPP on UNS S32003 at different concentrations of NaCl solution at 25°C.

The starting potential increases as the NaCl concentration decreases; this potential is a direct result of the open circuit potential (OCP) and indicates how the higher the NaCl concentration, the more active the surface after one hour of OCP monitoring. From the CPP graph, a passivity range of potential is identified that can be valid for every concentration. Three potentials were selected to test the material for PP, EIS, and Mott-Schottky analysis: 0.2 V, 0.5 V, and 0.8 V vs Ag/AgCl. These potentials in the passive region were selected to evaluate different possible reactions and arrangements of the passive layer.

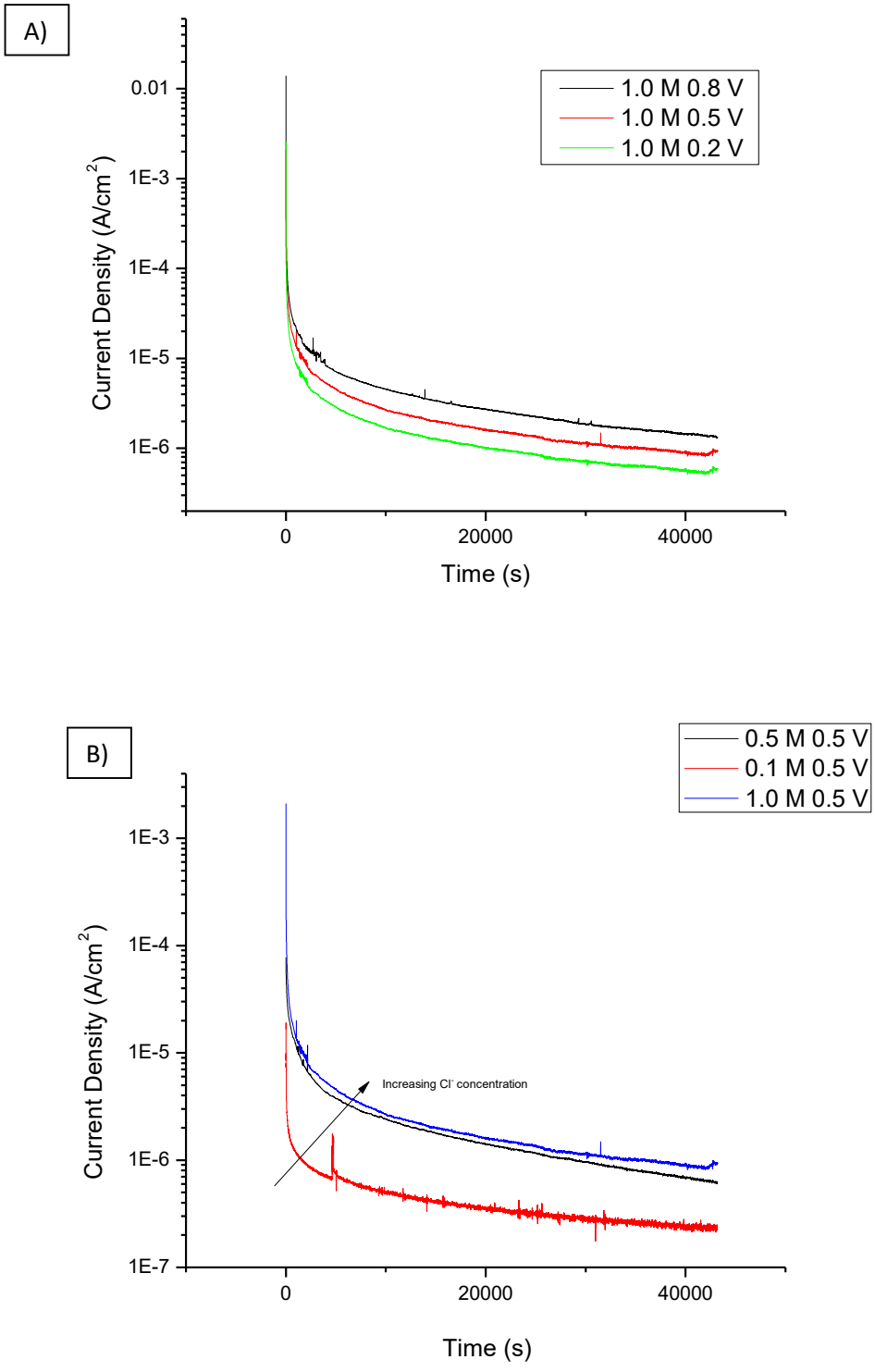

Figure 5.2. Potentiostatic tests showing a) the effect on applied potential and b) the effect of Cl^- concentration.

Under steady-state conditions, the polarization and chloride content of the solutions tends to increase the current density of the working electrode, as shown in Figure 5.2. This anodic current is directly proportional to the interfacial reaction occurring in the passive layer; since the passive nature of the alloy allows it to form protective barrier layers, no more direct oxidation occurs (as in that of a carbon steel, for example). Macdonald et al. [12] proposed that a set of interfacial kinetic reactions based on the movement of charge carrier species through a passive layer could predict the behavior of this layer and effectively evaluate the performance of the material. This leads to the argument that once all of the initial oxides are established, the current density reported in the potentiostatic tests is accomplished by the movement of the defects in the layer and therefore one needs to polarize the species for extended periods of time until it reaches a stable steady state. Figure 2(a) shows that naturally increasing the applied potential will result in higher current responses, as the metal is being "forced" to react and the kinetics of the interfacial reactions are modified; this kinetic stimulation can result in making a set of reactions more favorable than others. Elevated potentials provide the kinetic conditions to form Fe_2O_3, as opposed to unstable Fe_3O_4[26] [27], which, due to the difference in its crystallographic defects, will result in changes in the reaction process as a whole.

The lower the concentration of NaCl, the smaller the current density it achieves in this state; as seen in Figure 2 B, this relates to the capacity of the Cl^- to increase the rate of interfacial reactions. The 1.0 M and 0.5 M NaCl solutions have "aggressive" levels of chloride, which is why the current density in those solutions cannot reach the same level as that of 0.1 M NaCl.

5.2 Mott-Schottky analysis

J. Liu and D. D. Macdonald [28] found that the crystallography defect structure and the electronic properties of a pure metal are correlated, and the defects can be considered the charge carrier species. A Mott-Schottky analysis is then used to evaluate the electronic properties of the passive layer, assuming that this consideration applies to the passive layer formed in the UNS S32003 alloy. It is important to say that some formed oxides could be treated similarly to a pure metal, especially when considering that the chromium oxide layer is known to be only a few nanometers thick (about 15 layers of atoms) and is mostly comprised of Cr_2O_3, which is responsible for the passivity of a stainless steel. Many authors have found that the passive layer of stainless steel is usually comprised of a bi-layer system: a chromium barrier layer and another diffusive layer containing iron oxides and hydro-oxides and impurities [29].

According to the Mott-Schottky [11] theory, there are experimental relationships between the capacitance and the applied potential: the measured capacitance acts as a space charge capacitance and is analogous to the volume of the formed passive layer, assuming that the Helmholtz layer is negligible. For p-type semiconductors, the preponderant defects in the crystallographic structure are the cation vacancies, whereas n-type semiconductors have oxygen vacancies and/or cation interstitials. The equation is similar for both types of semiconductors, varying only in the sign that determines whether it is a donor or acceptor involved in the process. The relationships are given by

$$\frac{1}{C_{sc}^2} = \frac{2}{\varepsilon\varepsilon_0 q N_D}\left(V - V_{fb} - \frac{kT}{q}\right) \text{ for n-type}$$

and

$\frac{1}{C_{sc}^2} = -\frac{2}{\varepsilon\varepsilon_0 q N_A}(V - V_{fb} - \frac{kT}{q})$ for p-type,

where ε_0 is the vacuum permittivity (8.85 x 10^{-14} F/cm), e is the electron charge, ε is the dielectric constant of the oxide layer, k is the Boltzmann constant, T is the temperature in kelvin, V_{fb} is the flat band potential, and N_A and N_D are the concentrations of acceptors or donors, depending on the semiconductor type. It is important to note that this concentration of acceptors or donors is directly related to the concentration of defects, which could be useful for the PDM optimization; for the n-type, however, it is not possible to distinguish how many of those donors are attributed to the oxygen vacancies and how many to the cation interstitials. M.S.G Ferreira [30] studied the chromium effect on stainless steel alloys and contrasted it to pure iron, revealing that the addition of chromium alters the behavior of the passive film, creating a p-type effect in a naturally n-type layer of iron. The p-type behavior was attributed to the Cr_2O_3 passive film; the higher the concentration of chromium in the alloy, the more negative the slope becomes, i.e., the capacitance response of a p-type semiconductor increases. In contrast, above the flat band potential, the straight line representing the n-type behavior barely changes.

Figure 5.3 shows the Mott-Schottky plots for UNS S32003 tested under selected conditions. The kinetic effect of the applied potential is demonstrated in each plot: the samples that were polarized at 0.8 V vs Ag/AgCl for 12 hours could be subject to a wider range of potential to measure the AC polarization sweep, as seen in Figure 5.3 A, revealing the duplex behavior of the samples at potentials much higher than the flat

band potential. The negative slopes are attributed to the chromium oxide layer, whereas the positive slope that starts from the flat band potential is attributed to the n-type semiconductor of an iron-rich oxide layer. This duplex characteristic of the passive layer is expected across all of the samples; however, the potential at 0.5 V vs Ag/AgCl could not clearly show enough information about the appearance of the p-type semiconductor, as seen in Figure 5.3 B, although there is a zone after the initial linearity (at about 80 mV) that could be attributed to a change in semiconducting properties. The reason why samples polarized for 12 hours at 0.5 V and 0.1 V vs Ag/AgCl were not scanned at 0.8 V vs Ag/AgCl was to avoid changing the arrangement formed by the kinetics of the specific applied potential.

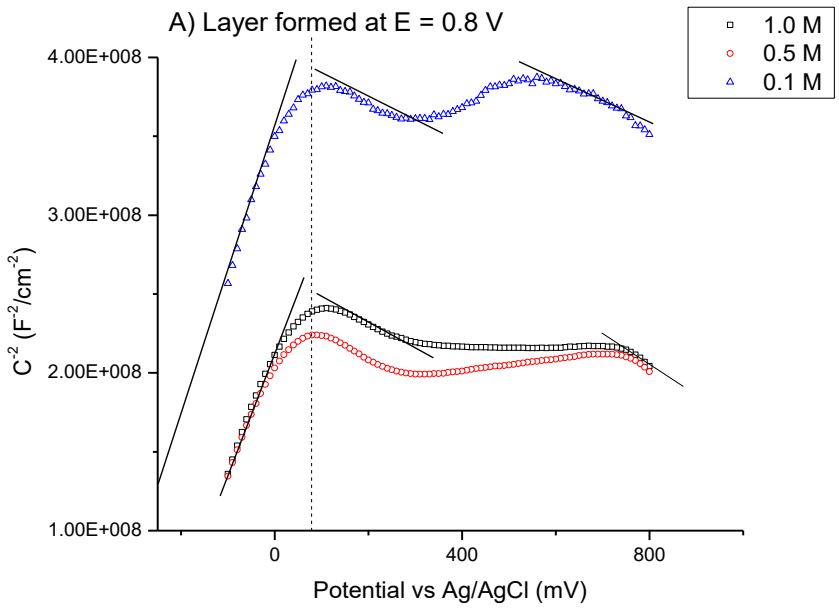

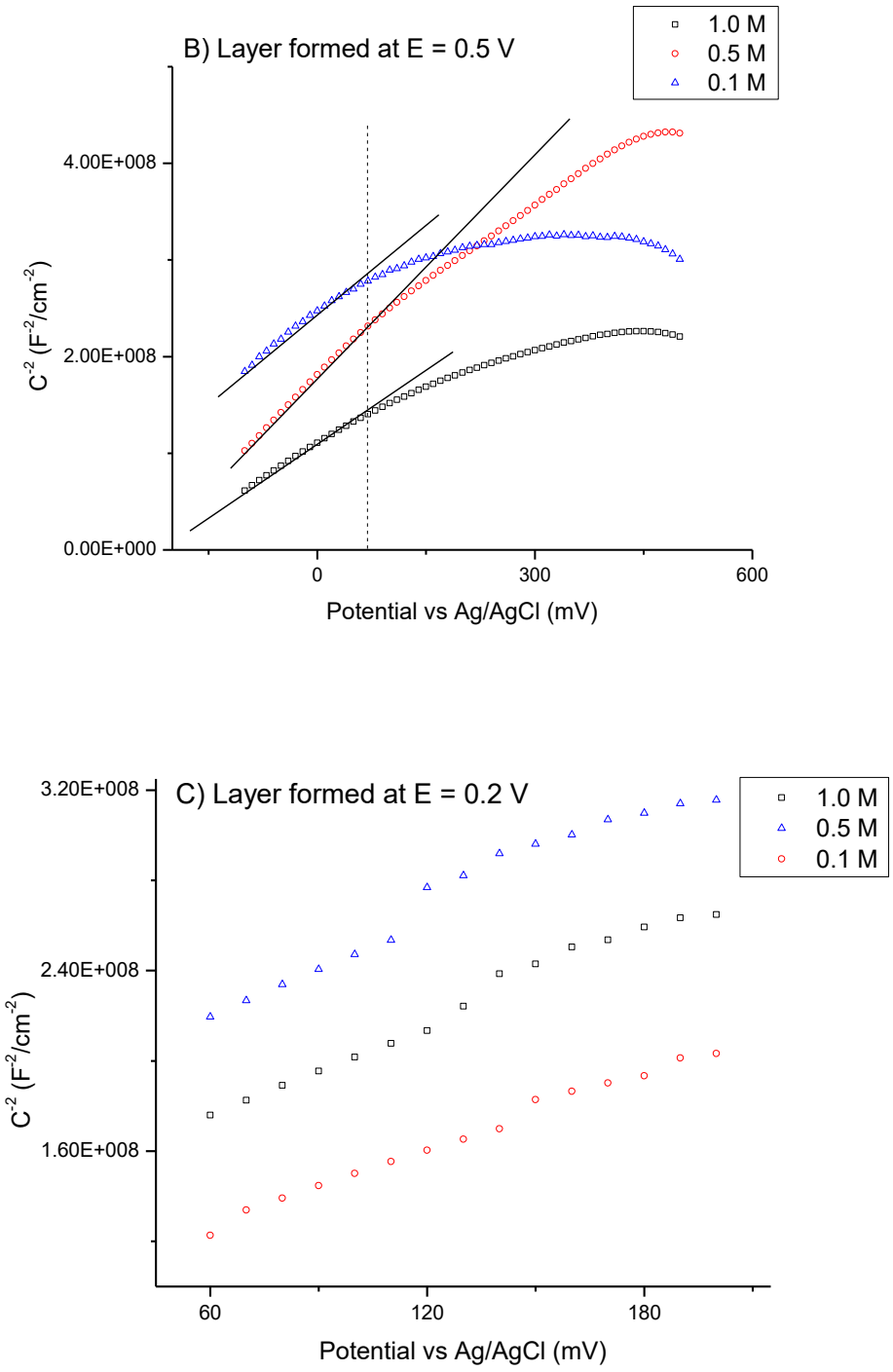

Figure 5.3. Mott-Schottky plots for passive layers formed at potentiostatic a) 0.8 V, b) 0.5 V and c) 0.2 V vs Ag/AgCl.

Following the kinetic effect of the applied potential, we could alter the range of the scan; the slope corresponding to the n-type zone of the curves did not change

significantly and was again repeated for 0.2 V vs Ag/AgCl of potentiostatic polarization, as shown in Figure 3 B. The overall slope was obtained and, using $\varepsilon = 12$ [31], N_A was estimated to be 3.58×10^{17} cm^{-3}, which is several orders of magnitude less than what is reported in the literature for other alloys.

SeJin Ahn et al. [23] studied the effects of chloride ions on the electronic properties of a p-type passive film on Ni; they concluded that a single chloride ion could be responsible for the cation interaction that leads to the accelerated vacancy generation rate and the vacancy concentration in the barrier layer. This findings may be comparable with those found in this work for the chromium oxide layer, as M. F. Montemor et al. [32] found that the formed chromium oxide layer on 316L stainless steels was a p-type semiconductor.

Considering the above studies, the mechanism proposed in this work is that of a system of bi-layer of chromium rich and iron-rich oxides is formed and the limiting process is found within the barrier layer, the chromium oxide layer. However, the chromium oxide layer is a p-type semiconductor, and the results of the Mott-Schottky analysis appear to disprove the idea that the preponderant defect is the cation vacancies, instead indicating that the predominant defects are either cation interstitials and/or oxygen vacancies, corresponding to a n-type semiconductor. Combining these ideas, the proposed mechanism would involve the interstitial movement of iron cations through the chrome-rich barrier layer as the limiting step. It can be argued that the Cr_2O_3, under ideal conditions, will prefer to have a p-type semiconducting behavior and will not readily promote the movement of negative charge carriers through it; however, the system is not comprised of a chromium/chromium oxide interface but rather a

metallic iron-rich/chromium oxide layer and therefore the idea of iron ion migration in chromium oxide is not far-fetched, especially when considering the stimulation of kinetics via the applied potential. In this proposed mechanism, the iron interstitials will tend to traverse through the chromium oxide, leaving behind a vacancy in the alloy/chrome-rich layer and reacting with the water of the chrome-rich layer/iron-rich layer that the iron-rich layer permeated. This mechanism is consistent with the idea of passivity breakdown due to accumulation of vacancies at the interface of the metal and the start of the passive layer; it also can allow for the growth of the iron-rich layer and it explains the meaning of such a low interstitial concentration, since the chromium-rich oxide layer will not hold the same electronic properties as an iron oxide layer.

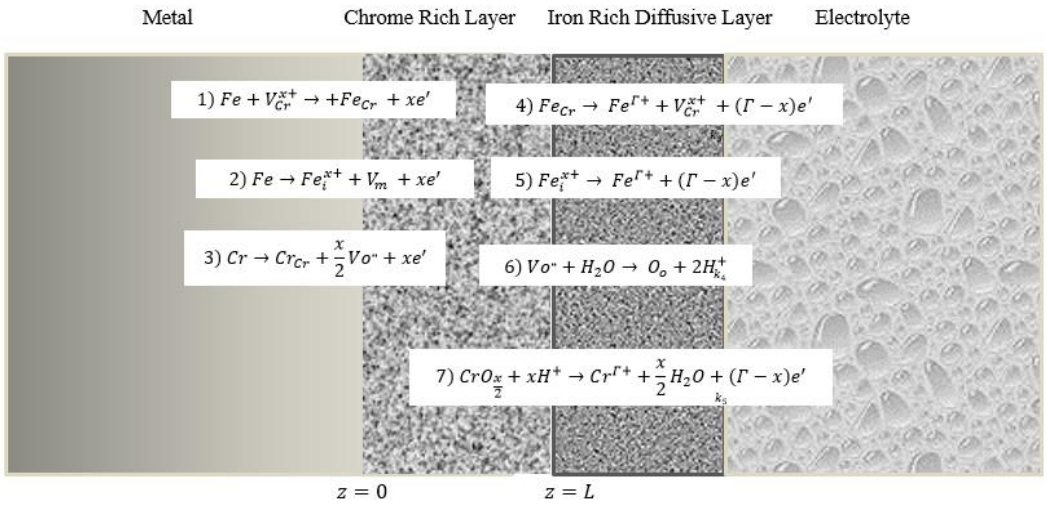

Figure 5.4. Schematic representation of processes occurring on the proposed passive layer.

To add experimental evidence to this model, XPS analysis was performed on selected samples. The effect of the applied potential was studied at a constant NaCl concentration. Figure 5 shows the results of the atomic percentage of each species as a function of depth; the region where oxygen is high represents the oxide layer. The sputtering time can be transformed to depth following the method of Nguyen et al. [33]

because Fe_2O_3 is 60% and Cr_2O_3 is 50% of the SiO_2 in the equipment's calibration. The depth in nm is proportional to the sputtering time in minutes; however, considering the presence of different oxides, as shown in the XPS analysis, no direct relationship can be confirmed. The chromium oxide layer, which is the one responsible for the protection of the metal, is about 15 layers of atoms deep according to [22] for most stainless steels, corresponding to about 2 nm, which is consistent with the results shown in the atomic profiles. Following the path of the chromium concentration, there is a maximum, a few nanometers into the passive layer, related to the barrier layer, while the rest of the passive layer can be considered a mixture of iron oxides. Figure 5 A reports an unusual amount of iron in the outermost part of the passive layer and an overall bigger zone of oxides; considering that the treatment was 0.8 V, it could be argued that due to the high potential applied, the second layer had a considerable growth of iron-rich oxides as opposed to the other treatments, as seen in Figure 5 B and C.

The growth of the second layer, mostly comprised of oxides and hydro-oxides of iron, was found and reported elsewhere [34], where the times of exposure where considerably larger. The assumption of a dynamic system of layers can lead to deviations when assessing the protective behavior of a passive metal, even if the iron-rich layer is permeable and not considered the rate-limiting step; the ohmic drop formed by it must be considered when constructing a PDM.

5.3 PDM proposed

The faradaic total impedance is a function of the reactions proposed in Figure 5.4 as well as the rest of the components that the charge has to go through for the entire system.

Since both the iron- and chromium-rich layers appear to be present, the proposed electric circuit predicts that the total impedance is given by the arrangement of the faradaic impedance generated by the transport of iron interstitials and oxygen vacancies and the geometric capacitance formed by the volume of the innermost barrier layer, followed by an RC circuit that accounts for the ohmic drop of the outermost diffusive layer and the bulk resistance of the electrolyte in series; the schematic of the system is shown in Figure 5.5.

The rate constants from the proposed point defect reactions can be given according to the activated complex theory [35].

- $k_1 = k_1^0 e^{a_1(v-R_l)} e^{-b_1 L}$ (5.1)
- $k_2 = k_2^0 e^{a_2(v-R_l)} e^{-b_2 L}$ (5.2)
- $k_3 = k_3^0 e^{a_3(v-R_l)}$ (5.3)
- $k_4 = k_4^0 e^{a_5(v-R_l)}$ (5.4)
- $k_6 = k_6^0 e^{a_6(v-R_l)}$ (5.5)
- $k_7 = k_7^0 e^{a_7(v-R_l)}$ (5.6)

Where $a_i = \frac{\alpha_i F}{RT}$ where α_i is the transfer coefficient, F is Faraday's constant, R is the ideal gas constant, and T is 298°K.

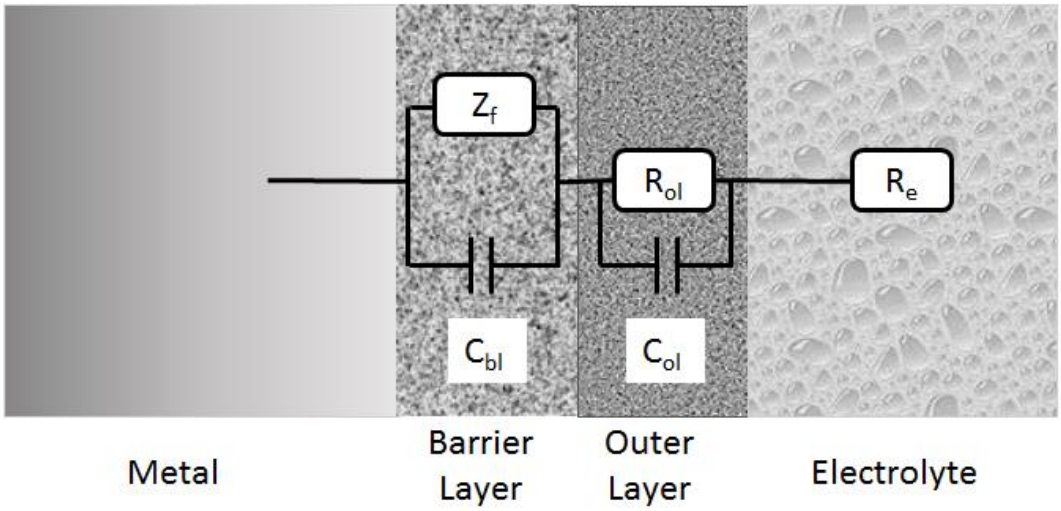

Figure 5.5. Equivalent circuit proposed for the total impedance.

All the contribution to the AC current can be given by the following equation:

$$I = F[xk_1\left(\frac{C_M^0}{C_M^{std}}\right) + xk_2 + xk_3 + (\Gamma - x)k_4 + (\Gamma - x)k_5\left(\frac{C_i^L}{C_i^{sli}}\right) + (\Gamma - x)k_7\left(\frac{C_H^L}{C_{Hstn}}\right)^n \quad (5.7)$$

For calculating the impedance:

$$\delta I = \left(\frac{\delta I}{\delta V}\right) dV + \left(\frac{\delta I}{\delta I}\right) dI + \left(\frac{\delta I}{\delta L}\right) dL + \left(\frac{\delta I}{\delta C_i^L}\right) dC_i^L \quad (5.8)$$

The objective becomes to obtain an expression for each of the partial derivatives.

$$\left(\frac{\delta I}{\delta V}\right) = F * (xk_1a_1C_M^0 + xk_2a_2 + xk_3a_3 + (\delta - x)k_4a_4 + (\delta - x)k_5a_5C_i^L + (\delta - x)k_7a_7C_H^n = I_V \quad (5.9)$$

Where C_M^0 is the dimensionless concentration of cation vacancies at x = 0, C_i^L is the dimensionless concentration of metallic interstitials at x = L or the barrier layer/outer layer interface, and C_H^n is the concentration of hydrogen ions across the system since it is considered to be constant.

$$\left(\frac{\delta I}{\delta L}\right) = -F * (xk_1 b_1 C_M^0 + xk_2 b_2 + xk_3 b_3) = I_L \quad (5.10)$$

$$\left(\frac{\delta I}{\delta I}\right) = -R_{OL} \left(\frac{\delta I}{\delta L}\right) = I_I \quad (5.11)$$

Where R_{0L} is the term associated with I*R_{0L} that described the potential drop across the outer layer.

$$\left(\frac{\delta I}{\delta C_M^0}\right) = F * (xk_1) = I_M^0 \quad (5.12)$$

$$\left(\frac{\delta I}{\delta C_i^L}\right) = F * \left((\delta - x)k_5\right) = I_i^L \quad (5.13)$$

In regards to the oxide growth:

$$\frac{dL}{dt} = \frac{dL^+}{dt} - \frac{dL^-}{dt} = \Omega k_3 - \Omega k_7 C_H^n \quad (5.14)$$

$$\frac{d\delta L}{dt} = \Omega \delta k_3 - \Omega \delta k_7 C_H^n \quad (5.15)$$

$$\frac{d\delta L}{dt} = \Omega(k_3 a_3 \delta V - k_3 a_3 R_{OL} \delta I - k_3 b_3 \delta L) - \Omega(k_7 a_7 R_{OL} \delta V - k_7 a_7 R_{OL} \delta I) C_H^n \quad (5.16)$$

If $\delta L = \Delta L\, e^{j\omega t}$

Then:

$$j\omega \Delta L = \Omega(k_3 a_3 \Delta V - k_3 a_3 R_{OL} \Delta I - k_3 b_3 \Delta L) - \Omega(k_7 a_7 \Delta V - k_7 a_7 R_{OL} \Delta I) C_H^n \quad (5.17)$$

Rearranging:

$$\frac{\Delta L}{\Delta V} = L_V + L_I \frac{\Delta I}{\Delta V} \tag{5.18}$$

Where:

$$L_V = \frac{\Omega(k_3 a_3 - k_7 a_7 C_H^n)}{j\omega + \Omega k_3 b_3} \tag{5.19}$$

$$L_I = -L_V R_{OL} \tag{5.20}$$

In regards to the transport of metallic interstitials across the barrier oxide layer.

$$\left(\frac{dC_i^L}{dt}\right) = k_5 C_i^L \tag{5.21}$$

$$\left(\frac{d\delta C_i^L}{dt}\right) = \delta k_5 C_i^L = k_5 a_5 C_i^L \delta V - k_5 a_5 C_i^L R_{OL} \delta I - k_5 \delta C_i^L \tag{5.22}$$

$$j\omega \Delta C_i^L = k_5 a_5 C_i^L \Delta V - k_5 a_5 C_i^L R_{OL} \Delta I - k_5 \Delta C_i^L \tag{5.23}$$

$$\left(\frac{\Delta C_i^L}{\Delta V}\right) = C_{iV}^L + C_{iI}^L \frac{\Delta I}{\Delta V} \tag{5.24}$$

Considering that $C_i^L = \frac{k_2}{k_5}$ at steady state because of conservation of production and annihilation of metallic interstitials.

$$C_{IV}^L = \frac{k_2 a_5}{j\omega + k_5} \tag{5.25}$$

$$C_{iI}^L = -C_{IV}^L R_{OL} \tag{5.26}$$

Similarly, for the cation vacancies:

$$\left(\frac{dC_M^0}{dt}\right) = k_1 C_M^0 \tag{5.27}$$

$$\left(\frac{dC_M^0}{dt}\right) = \delta k_1 C_M^0 = k_1 a_1 C_M^0 \delta V - k_1 a_1 C_M^0 R_{OL} \delta I - k_1 \delta C_M^0 \tag{5.28}$$

$$j\omega \Delta C_M^0 = k_1 a_1 C_M^0 \Delta V - k_1 a_1 C_M^0 R_{OL} \Delta I - k_1 \Delta C_M^0 \tag{5.29}$$

$$\left(\frac{\Delta C_M^0}{\Delta V}\right) = C_{MV}^0 + C_{MI}^0 \frac{\Delta I}{\Delta V} \tag{5.30}$$

Where at steady state $C_M^0 = \frac{k_4}{k_1}$ then:

$$C_{MV}^0 = \frac{k_4 a_1}{j\omega + k_1} \tag{5.31}$$

$$C_{MI}^0 = -C_{MV}^0 * R_{OL} \tag{5.32}$$

The admittance is:

$$\frac{\Delta I}{\Delta V} = I_V + I_I \frac{\Delta I}{\Delta V} + I_L \frac{\Delta L}{\Delta V} + I_i^L \frac{\Delta C_i^L}{\Delta V} + I_M^0 \frac{\Delta C_M^0}{\Delta V} \tag{5.33}$$

$$\frac{\Delta I}{\Delta V} = I_V + I_I \frac{\Delta I}{\Delta V} + I_L [L_V + L_I \frac{\Delta I}{\Delta V}] + I_i^L [C_{iV}^L + C_{iI}^L \frac{\Delta I}{\Delta V}] + I_M^0 [C_{MV}^0 + C_{MI}^0 \frac{\Delta I}{\Delta V}] \tag{5.34}$$

Solving for $\frac{\Delta I}{\Delta V}$ yields the final expression for the Faradaic Admittance:

$$\frac{\Delta I}{\Delta V} = \frac{I_V + I_L L_V + I_i^L C_{iV}^L + I_M^0 C_{MV}^0}{1 - [I_I + I_L L_I + I_i^L C_{iI}^L + I_M^0 C_{MI}^0]} \tag{5.35}$$

The terms $L_V, L_I, C_{iV}^L, C_{iI}^L, C_{MV}^0,$ and C_{MI}^0 are all dependent on jω and contain imaginary numbers that allow for adaptation to the capacitive response. The terms L_V and L_I are associated with the steady-state thickness, C_{iV}^L *and* C_{iI}^L refer to the formation and annihilation of interstitial species at the oxide layer/barrier layer interface, and lastly C_{MV}^0, and C_{MI}^0 formation and annihilation of cation vacancies at the metal/barrier layer interface, respectively.

5.4 Optimization of the PDM model based on EIS experimental data

Ellis2 software contained the algorithm to optimize a function to the experimental data; the code that contains the description of the function as well as all the variables can be found in the appendix.

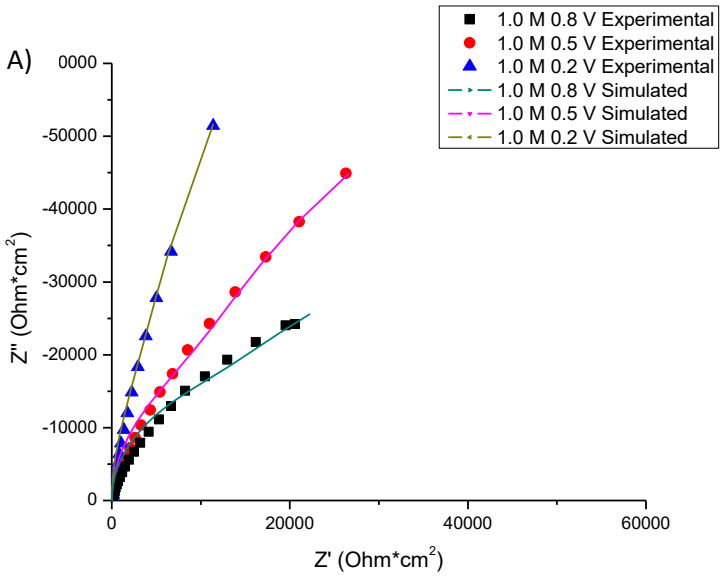

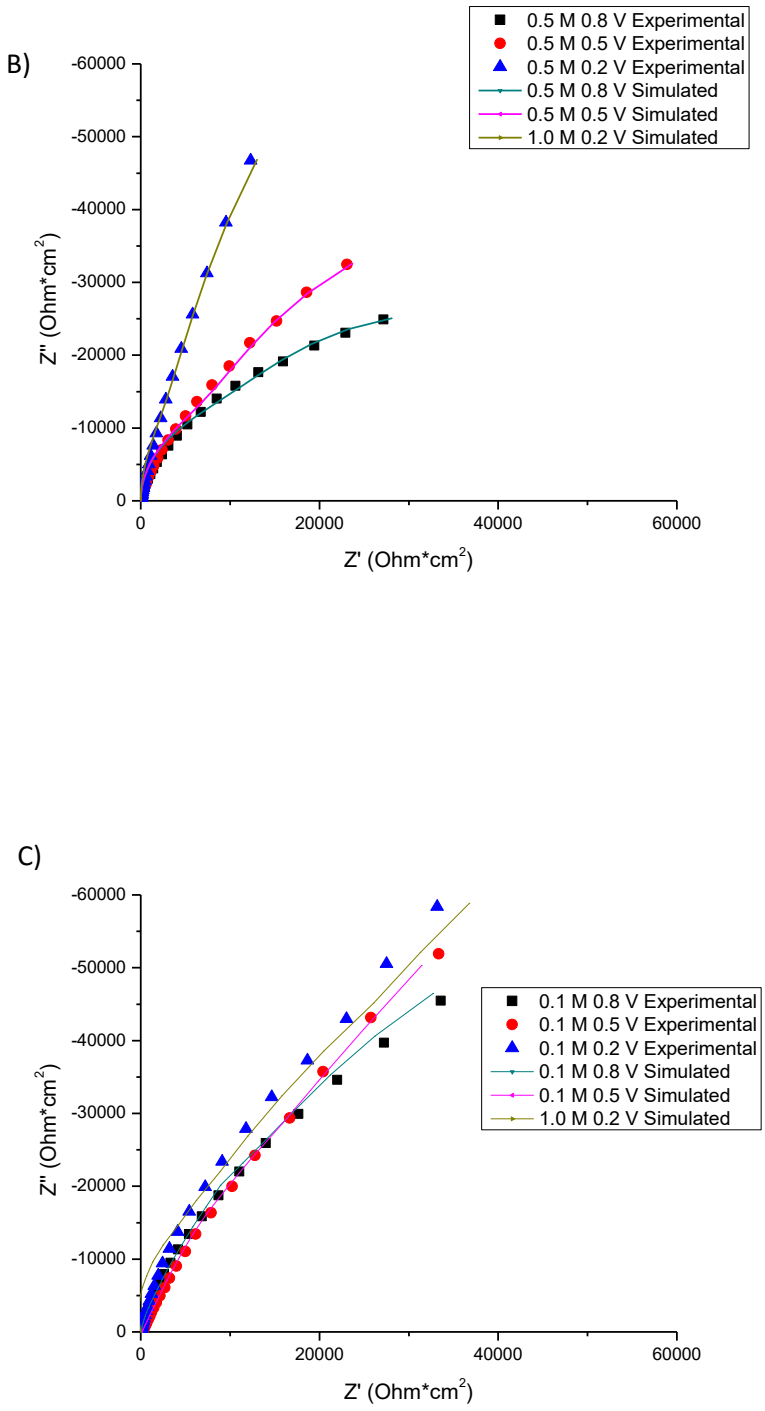

Figure 5.6. Fitting of EIS by the PDM proposed Nyquist plot a) 1.0 M b) 0.5 M c) 0.1 M NaCl.

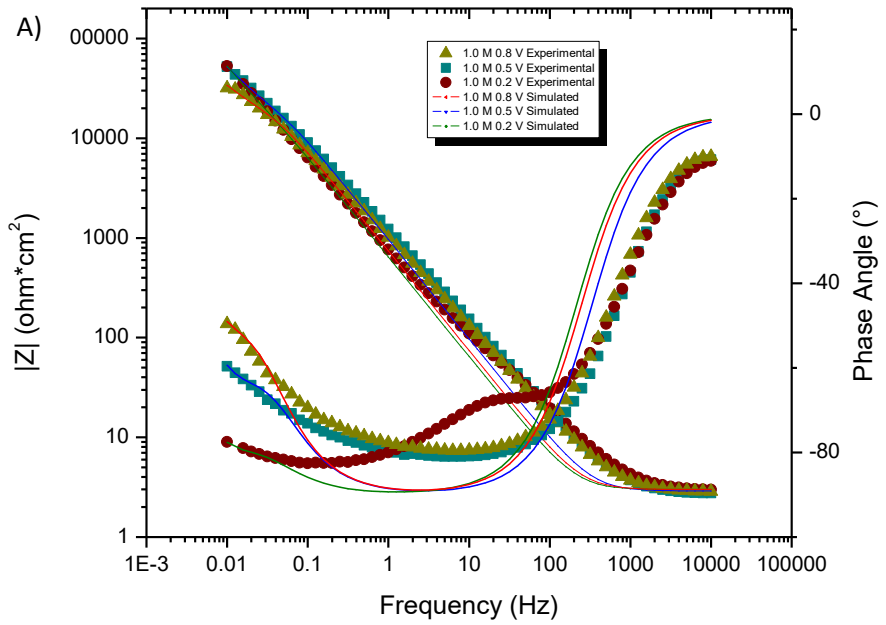
A)
1.0 M 0.8 V Experimental
1.0 M 0.5 V Experimental
1.0 M 0.2 V Experimental
1.0 M 0.8 V Simulated
1.0 M 0.5 V Simulated
1.0 M 0.2 V Simulated
|Z| (ohm*cm2)
Phase Angle (°)
Frequency (Hz)
00000
10000
1000
100
10
1
0
-40
-80
1E-3
0.01
0.1
1
10
100
1000
10000
100000

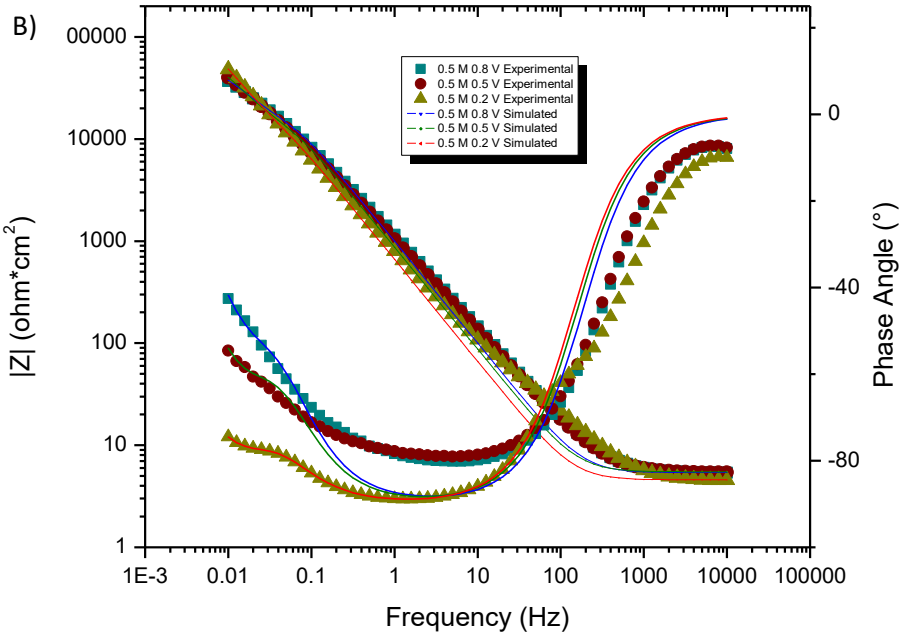
B)
0.5 M 0.8 V Experimental
0.5 M 0.5 V Experimental
0.5 M 0.2 V Experimental
0.5 M 0.8 V Simulated
0.5 M 0.5 V Simulated
0.5 M 0.2 V Simulated
|Z| (ohm*cm2)
Phase Angle (°)
Frequency (Hz)
00000
10000
1000
100
10
1
0
-40
-80
1E-3
0.01
0.1
1
10
100
1000
10000
100000

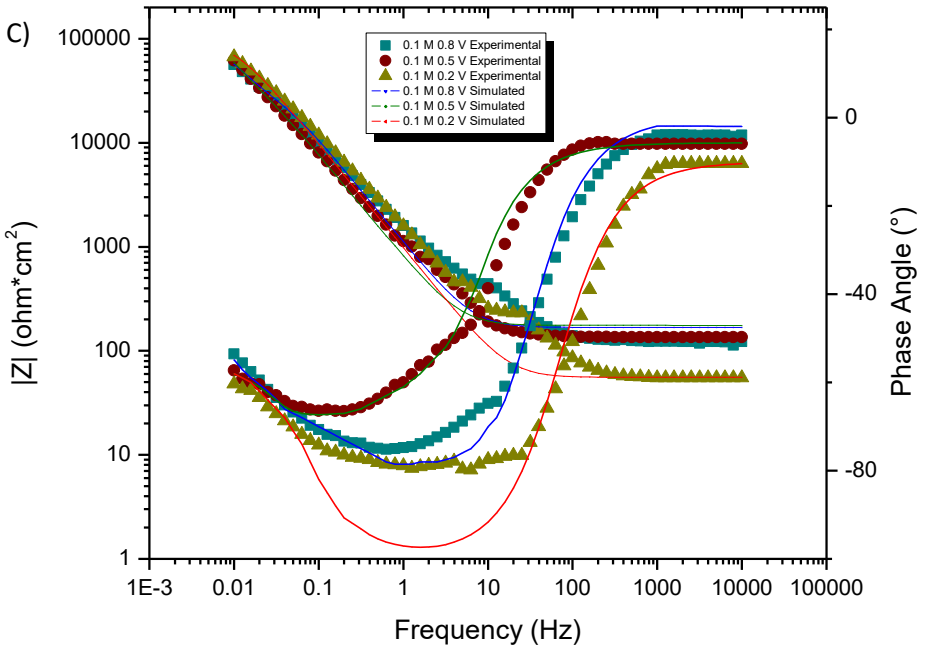

Figure 5.7. Fitting of EIS by the PDM Bode plot a) 1.0 M b) 0.5 M c) 0.1 M in NaCl.

Figures 5.6 and 5.7 show the Nyquist, Bode, and phase angle diagrams of the response to EIS under experimental conditions. This time, the previously-developed PDM equation was fit; the results of the parameters obtained by the fitted equations are shown in Table 4.1. An explanation to the experimental behavior of the system to EIS testing was given in chapter three; in conclusion, as the chloride concentration increased, the potential that was held increased, the overall magnitude of the impedance decreased, and the capacitance term decreased, which means that the electrochemical process is accelerating. This is in agreement with the idea of the "aggressiveness" of the environment and the "acceleration" to the natural process given by providing an elevated difference in potential to the working electrode.

In this chapter, the results obtained from optimizing the PDM will be covered thoroughly. In Table 4.1, the first terms are described as “alpha”, which is the transfer coefficient for each independent reaction; this is indicative of the amount of charge being contributed by this half-reaction to the overall reaction. Since all of the half-reactions proposed in the PDM are oxidations, naturally the reduction reaction that will be associated with that will be (α-1).

The polarizability α (without subscript) of the barrier oxide layer affects all the reactions. α is the result that is obtained from the activity term a_i, as indicated in the following equation:

$$a_i = x\alpha_i(1-\alpha)\frac{F}{R*T} \tag{5.36}$$

The term marked as “eps” comes from epsilon, the Greek letter ε, and it usually represents the electric field strength of an electrochemical double layer; in this case, there is no such thing, since the Helmholtz layer requires that ions in a solution become arranged by the surface of a charged electrode. In this case, the reactions across the barrier layer are dictated by the production, transport, and annihilation of point defects, and thus the electric field is formed on the solid geometry of the barrier layer and assumed to be constant and independent of the applied potential [36].

The terms Cbl and Col are the capacitance due to the volume of the barrier layer and the outer layer, respectively. Rol is the resistance of the outer layer and is also used for the faradic impedance, since I*Rol represents the ohmic drop generated by the outer layer. I*Rol is very important and also parallel to the resistance to charge transport obtained in chapter three. R_e is the resistance generated by the electrolyte. A schematic

configuration of the electric analogue can be seen in Figure 5.4, where Z_f is the inverse of the admittance that was derived in section 5.3.

CH0, CM0, and CIL are the dimensionless concentrations equivalent to C_H^0, C_M^0, C_I^L that were used to develop the PDM. These values are intrinsically related to the generation, transport, and annihilation of oxygen vacancies, cation vacancies, and interstitials, respectively. The term "ohm" is the volume per mole of cations in the barrier layer. K_i is the rate constant of each reaction postulated for the PDM.

Table 5.1. Results from the optimization of the proposed PDM.

	0.1 M			0.5 M			1.0 M		
	0.2 V	0.5 V	0.8 V	0.2 V	0.5 V	0.8 V	0.2 V	0.5 V	0.8 V
alpha1	4.25E-01	3.22E-01	2.59E-01	4.83E-01	2.64E-01	1.79E-01	2.40E-01	4.18E-01	4.59E-01
alpha4	5.26E-01	1.03E-01	2.21E-01	7.04E-03	1.43E-02	4.27E-01	2.32E-01	9.10E-02	2.93E-01
alpha7	5.93E-01	2.64E-01	4.16E-01	2.64E-01	3.49E-01	3.54E-01	2.38E-01	4.52E-03	0.305543
Polarizability	2.05E-01	7.01E-01	2.98E-01	7.79E-01	7.48E-01	9.76E-01	9.05E-01	5.08E-01	6.67E-01
eps	1.00E+06	1.00E+06	1.00E+06	1.00E+06	1.00E+06	1.00E+06	1.00E+06	1.00E+06	1.00E+06
Cbl	2.26E-04	4.78E-04	2.01E-04	2.40E-04	4.09E-04	4.31E-04	2.46E-04	3.30E-04	6.28E-04
K1	8.99E-09	9.12E-09	2.53E-08	3.32E-08	8.20E-08	7.01E-07	9.57E-07	6.94E-06	5.58E-06
K2	8.41E-07	7.10E-07	9.09E-07	7.16E-07	6.09E-07	9.93E-07	9.47E-07	9.41E-07	1.19E-06
K3	6.54E-07	6.87E-07	2.93E-07	5.16E-07	8.84E-07	2.99E-07	5.24E-07	3.90E-07	9.31E-07
K4	6.74E-08	8.66E-08	1.99E-07	6.40E-07	9.22E-07	7.59E-07	5.21E-07	9.09E-06	3.88E-06
K5	5.35E-07	7.09E-08	3.79E-08	2.68E-07	5.11E-07	5.98E-07	8.96E-07	2.79E-06	2.96E-06
K7	5.50E-07	5.74E-07	4.83E-07	3.06E-07	4.87E-07	5.50E-07	1.38E-07	2.27E-06	1.65E-06
CHN	4.83E-01	8.36E-01	7.45E-01	2.74E-01	2.80E-01	3.97E-01	1.26E-01	7.87E-01	6.39E-02
CM0	6.75E-01	6.11E-01	6.10E-01	7.15E-01	8.39E-01	8.66E-01	7.24E-01	7.53E-01	7.49E-01
CIL	3.95E-01	6.57E-01	3.19E-01	8.17E-01	4.84E-01	8.96E-01	2.88E-01	5.38E-01	6.68E-01
Rol	9.61E+03	1.95E+04	9.52E+04	4.73E+04	8.62E+03	1.10E+04	8.44E+04	1.15E+04	1.45E+04
Col	3.45E-04	2.89E-04	5.06E-04	6.81E-04	3.29E-04	2.53E-04	6.90E-01	3.27E-04	3.25E-04

As mentioned in section 5.2, the preponderant defect found on the barrier layer was the cation vacancies; therefore, special attention is to be given to reaction rates that involve p-type semiconducting reactions. Figure 5.9 shows the evolution of k_1 and k_4 with respect to the chloride ion concentration; reactions 1 and 4 are associated with the

generation and annihilation of cation vacancies, respectively. Reaction 4 in particular involves the production of cation vacancies. The mechanism involving the production of this species is the dissolution of a cation in a cation site that is exposed to the electrolyte, leaving behind a cation vacancy. This dissolution could be the product of a second oxidation that will take cation species to a δ oxidation state, i.e., producing (δ-x) electrons for the half-reaction, but alternatively the cation may simply be attracted by other negatively-charged species into the solution, resulting in the generation of a cation vacancy, but no charge transfer is associated in this case. Fortunately, at steady state, reactions 1 and 4 are associated with each other, with the relationship $C_M^0 = \frac{k_4}{k_1}$ and values of k_4 can be directly obtained from the model.

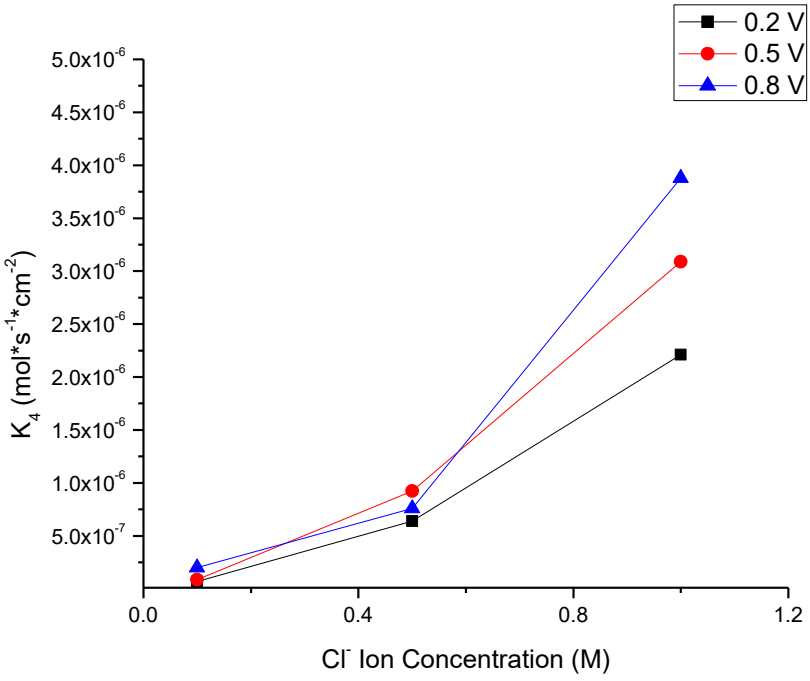

Figure 5.8. Evolution of rate constant K_4 with respect to Cl^- concentration.

Taking into consideration the effect of chlorides, i.e., favoring the production of cation vacancies because of their atomic size and electronegativity, it is natural to find

higher values of C_M^0 as the chloride concentration increases. Interestingly, 0.5 M NaCl had the highest number in this regard, which can be explained by considering that in the 1.0 M concentration, the amount of Cl^- ions is so high as to interfere with one another in the diffusion and adsorption process that leads to the generation of vacancies.

On the other hand, there are also the n-type semiconducting charge carrier reactions that can take place in the system. As seen in chapter four, the bi-layer system is not comprised of two homogenous phases, but rather a combination of these species. The inner-most layer is rich in chromium, so p-type behavior is expected to be predominant, but it gets richer in iron as it approaches the electrolyte. In other words, there is always the hetero-conjunction behavior in the oxide system of layers, hence the use of an all-inclusive PDM. Reactions 2 and 3 are associated with the generation of cation interstitials and oxygen vacancies. Reactions 5 and 6 involve the annihilation of these defects; however, reaction 6 cannot be described by the PDM, since no charge transfer is involved in this reaction though steady state is related to reaction 3.

Figure 5.9 shows the dependency of rate constants k_2, k_3, k_5, and k_7. k_2 and k_3 are rate constants of reactions that involve defect generation, specifically of metallic interstitials and oxygen vacancies, and thus they contribute to passivity breakdown as donors of charge, behaving as an n-type semiconductor. Since these reactions take place at the metal/barrier layer interface, no effect of the medium concentration is expected at steady state; as seen in Figure 5.9 A and B, there is little effect on the applied potential, which indicates that the current is mostly passing through reactions 1 and 4 in the form of an acceptor of charge, and the applied potential is mostly affecting the production of cation vacancies, rather than metallic interstitials and oxygen vacancies. Reaction

constants k_5 and k_6 involve the annihilation of defects generated in reactions 2 and 3, and they occur at the barrier layer/outer layer interface. At steady state, the chloride ion concentration appears to have a certain effect on reaction 5, as depicted in Figure 5.9 C, which can be explained by considering that it involves a further oxidation of the interstitial specie at the barrier layer/outer layer interface; the rate of reaction of this oxidation can be assisted by the electronegativity of the chloride ions at the interface where it occurs. Reaction 6 describes the annihilation of oxygen vacancies, which involves no charge transfer, and so this reaction would not be detected by the electrochemical technique and thus no effect of the chloride ions can be seen, although the production of hydrogen ions in reaction 6 could attract chloride ions to the barrier layer/outer layer interface to preserve electro-neutrality, contributing to the acceleration in the rates of reactions 4 and 5.

A)

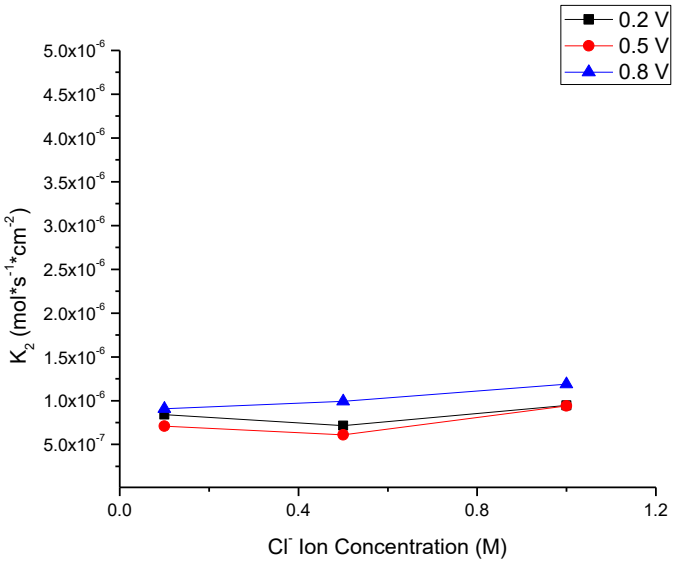

B)

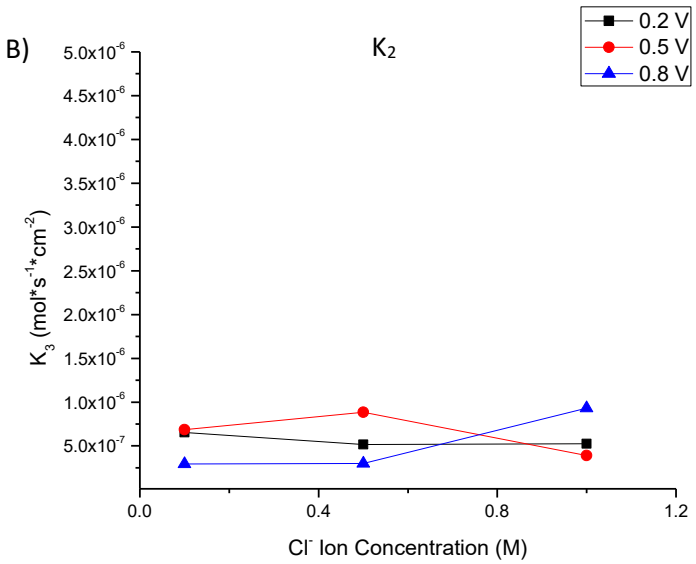
K2
0.2 V
0.5 V
0.8 V
5.0x10-6
4.5x10-6
4.0x10-6
3.5x10-6
3.0x10-6
2.5x10-6
2.0x10-6
1.5x10-6
1.0x10-6
5.0x10-7
K3 (mol*s-1*cm-2)
0.0
0.4
0.8
1.2
Cl- Ion Concentration (M)

C)

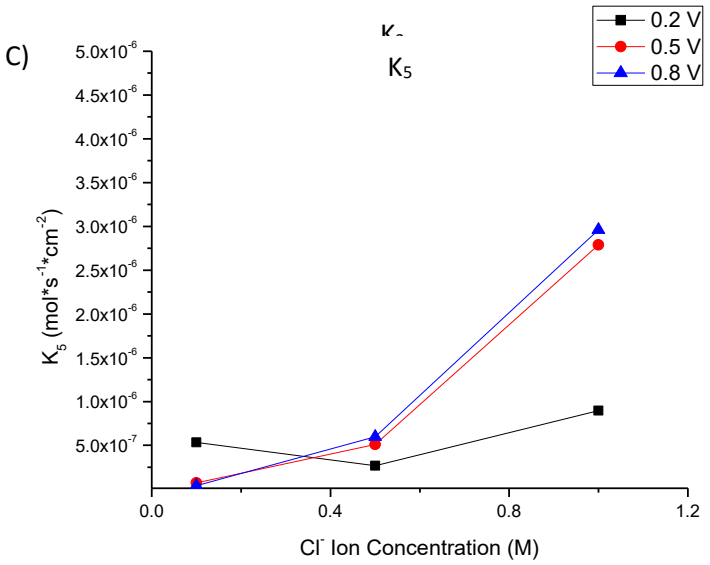
K5
0.2 V
0.5 V
0.8 V
5.0x10-6
4.5x10-6
4.0x10-6
3.5x10-6
3.0x10-6
2.5x10-6
2.0x10-6
1.5x10-6
1.0x10-6
5.0x10-7
K5 (mol*s-1*cm-2)
0.0
0.4
0.8
1.2
Cl- Ion Concentration (M)

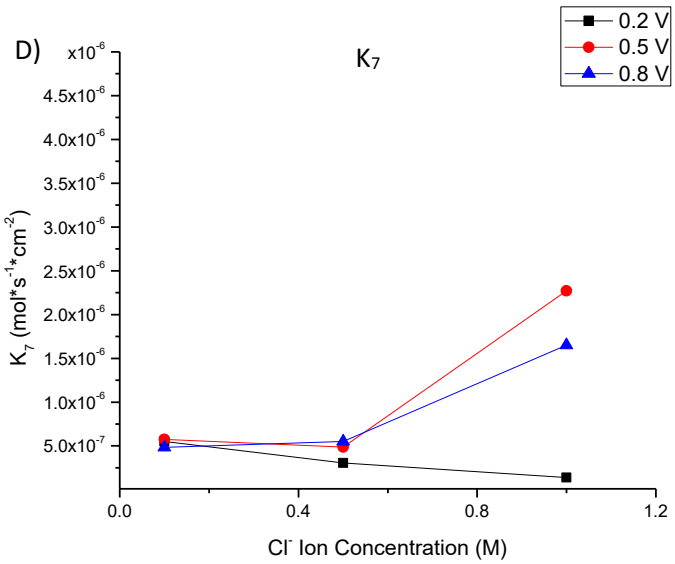

Figure 5.9. Dependency of the rate constants of the reaction discussed to the chloride ion concentration a) k_2, b) k_3, c) k_5 and d) k_7.

Figure 5.10 is a 2-D schematic representation of the reaction taking place as well as the interaction with chloride ions. As proposed in the PDM assumptions, reaction 2 can take place for both chromium and iron interstitial defect generation; more importantly, for reaction 1, both the iron and chromium are proposed to be responsible for the annihilation of cation vacancies.

Several advantageous arguments can be given to support this theory. Firstly, there is the thermodynamic likelihood of an iron cation to take a chromium cation site; both of them have similar atomic size and they can adopt the same oxidation states. The electron configuration at their d orbitals can be troublesome because of how differently chromium behaves than iron; however, when oxidized, they differ less from each other. Another advantage is the fact that the outer layer is rich in iron oxide, which may be outer-most because of the reaction's faster kinetics; however, growth of the second layer, the iron-rich layer is possible by the movement of iron species through the

chromium-rich barrier oxide layer. One last advantage is that the availability of chromium may be limited due to the relatively low contents of chromium added to the alloy, making it difficult to replenish the barrier layer and annihilate cation vacancies; therefore, when vacancies arrive at the metal/barrier layer interface, they are likely to react with compatible species such as the iron, which is vastly abundant.

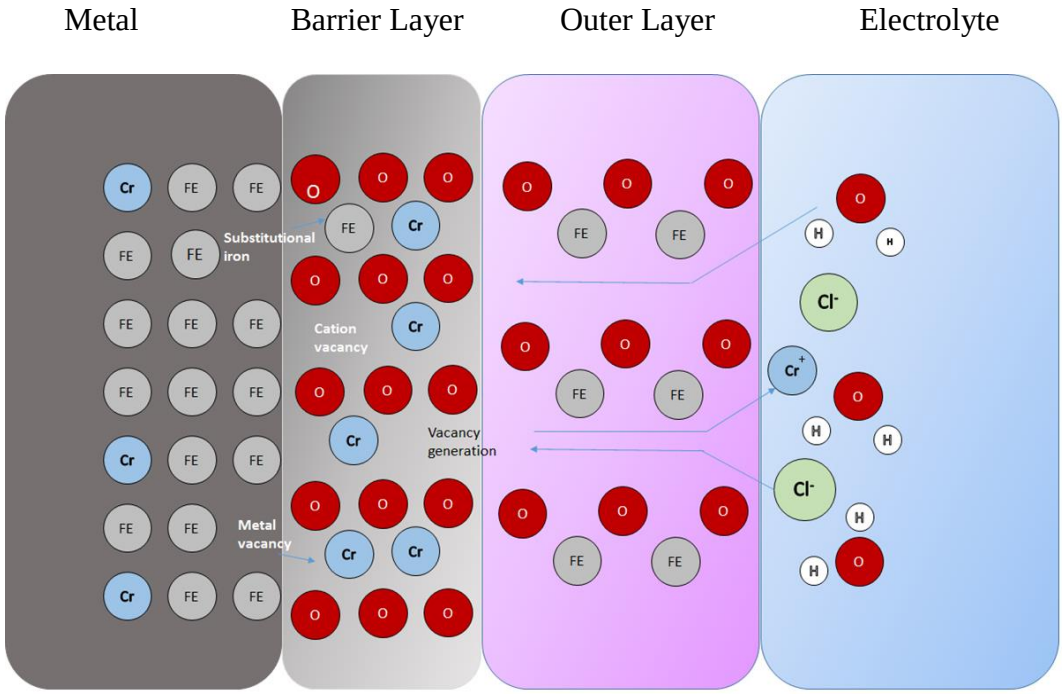

Figure 5.10 Mechanism and rate constant effects on the alloy.

Considering the amount of time the samples were polarized until they reached the steady state, the accelerated formation of cation vacancies had already taken place. An equilibrium is found and established as a charge carrier transport regime. Vacancy accumulation is also possible, which, in terms of integrity, is known to lead to breakdown of the passive layer, as explained previously.

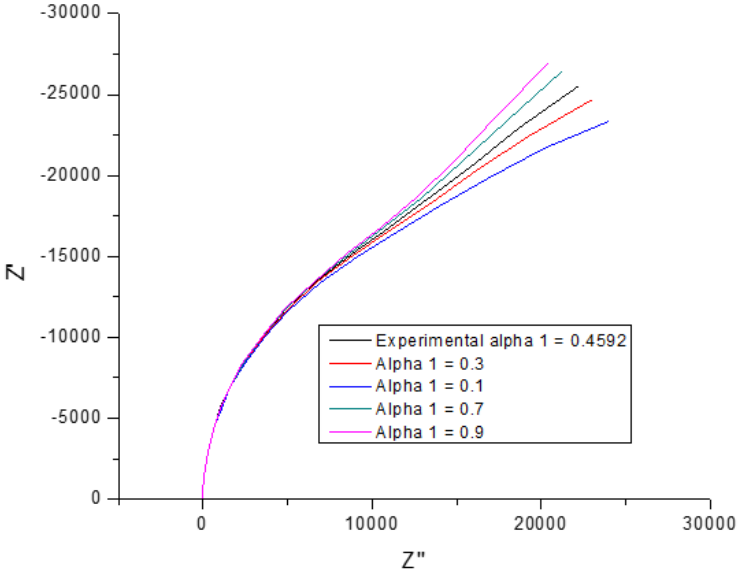
-30000
-25000
-20000
-15000
-10000
-5000
0
Z'
0
10000
20000
30000
Z"
Experimental alpha 1 = 0.4592
Alpha 1 = 0.3
Alpha 1 = 0.1
Alpha 1 = 0.7
Alpha 1 = 0.9

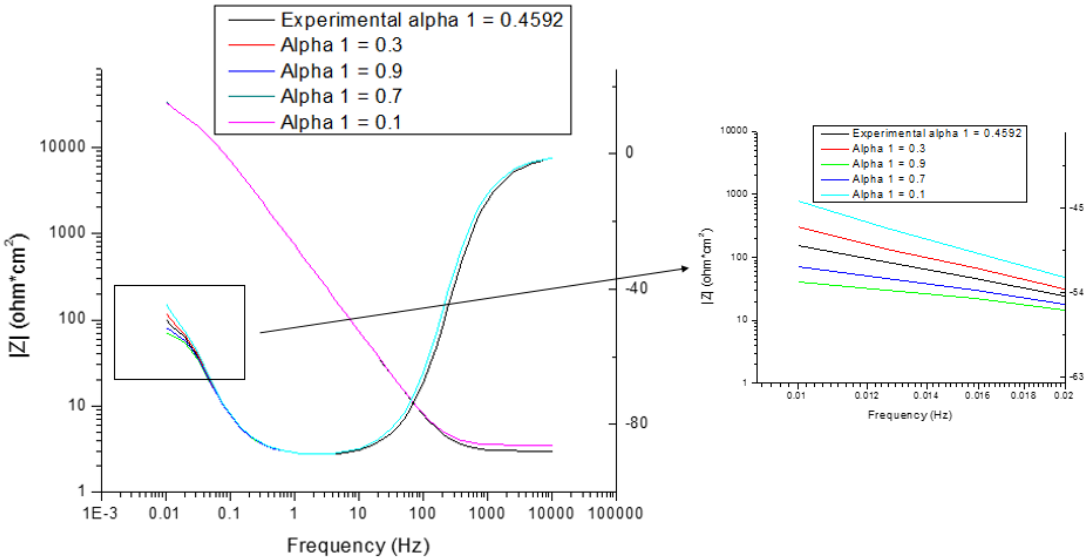
Experimental alpha 1 = 0.4592
Alpha 1 = 0.3
Alpha 1 = 0.9
Alpha 1 = 0.7
Alpha 1 = 0.1
|Z| (ohm*cm²)
10000
1000
100
10
1
0
-40
-80
1E-3
0.01
0.1
1
10
100
1000
10000
100000
Frequency (Hz)
Experimental alpha 1 = 0.4592
Alpha 1 = 0.3
Alpha 1 = 0.9
Alpha 1 = 0.7
Alpha 1 = 0.1
|Z| (ohm*cm²)
10000
1000
100
10
1
-45
-54
-63
0.01
0.012
0.014
0.016
0.018
0.02
Frequency (Hz)

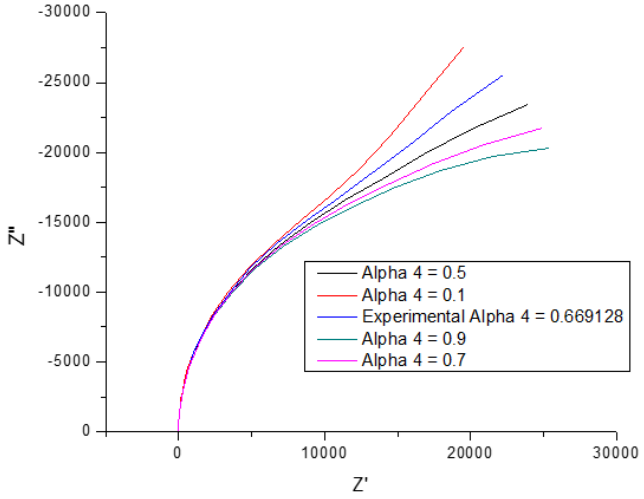
-30000
-25000
-20000
-15000
-10000
-5000
0
Z''
0
10000
20000
30000
Z'
Alpha 4 = 0.5
Alpha 4 = 0.1
Experimental Alpha 4 = 0.669128
Alpha 4 = 0.9
Alpha 4 = 0.7

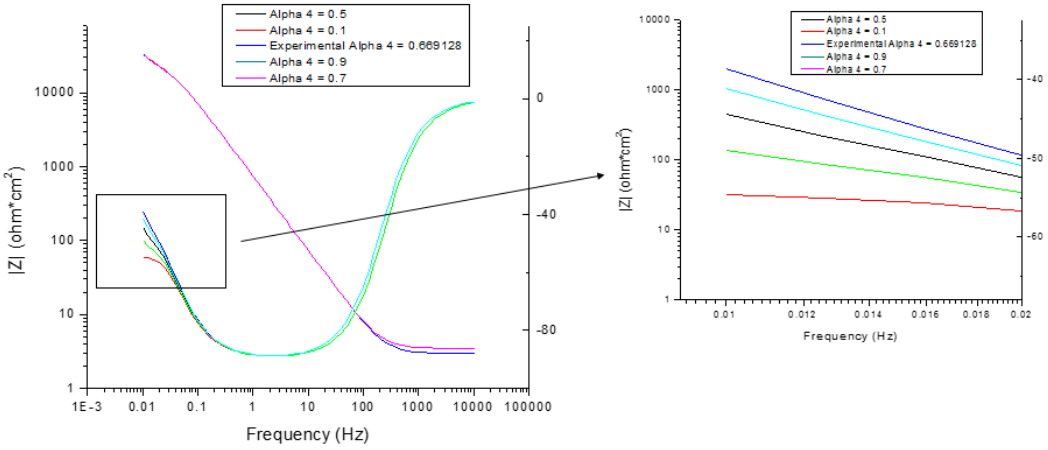
Alpha 4 = 0.5
Alpha 4 = 0.1
Experimental Alpha 4 = 0.669128
Alpha 4 = 0.9
Alpha 4 = 0.7
|Z| (ohm*cm²)
10000
1000
100
10
1
0
-40
-80
1E-3
0.01
0.1
1
10
100
1000
10000
100000
Frequency (Hz)
-40
-50
-60
0.01
0.012
0.014
0.016
0.018
0.02

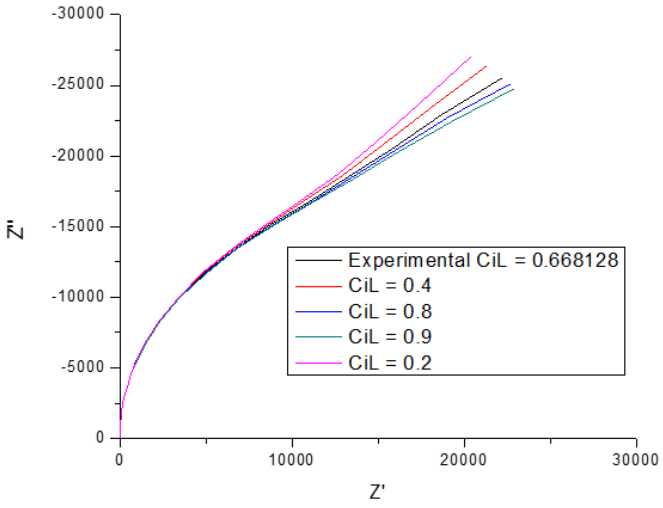
-30000
-25000
-20000
-15000
-10000
-5000
0
Z''
0
10000
20000
30000
Z'
Experimental CiL = 0.668128
CiL = 0.4
CiL = 0.8
CiL = 0.9
CiL = 0.2

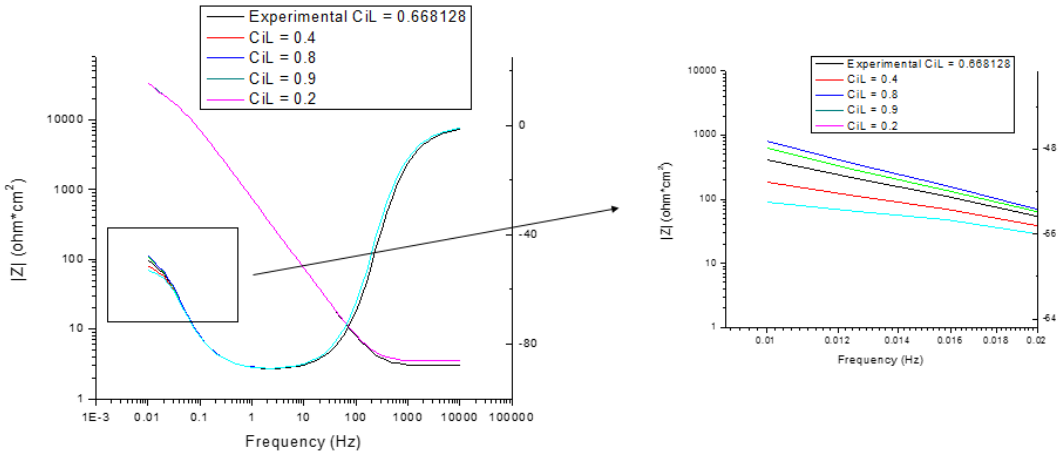
Experimental CiL = 0.668128
CiL = 0.4
CiL = 0.8
CiL = 0.9
CiL = 0.2
|Z| (ohm*cm²)
10000
1000
100
10
1
0
-40
-80
1E-3
0.01
0.1
1
10
100
1000
10000
100000
Frequency (Hz)
Experimental CiL = 0.668128
CiL = 0.4
CiL = 0.8
CiL = 0.9
CiL = 0.2
|Z| (ohm*cm²)
10000
1000
100
10
1
-48
-56
-64
0.01
0.012
0.014
0.016
0.018
0.02
Frequency (Hz)

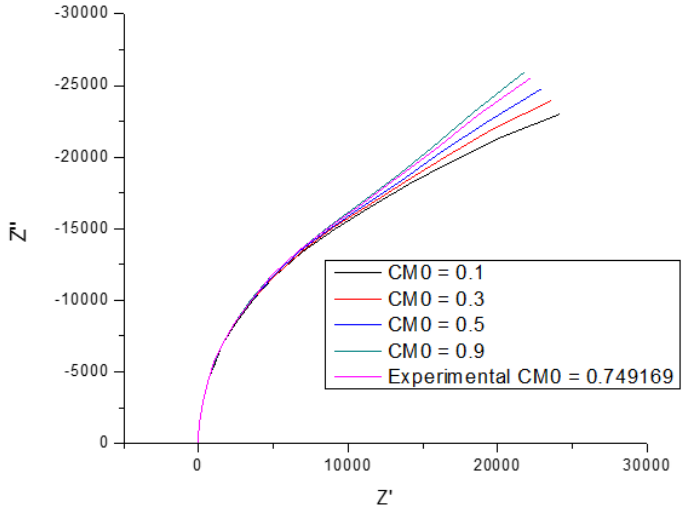
-30000
-25000
-20000
-15000
-10000
-5000
0
Z''
0
10000
20000
30000
Z'
CM0 = 0.1
CM0 = 0.3
CM0 = 0.5
CM0 = 0.9
Experimental CM0 = 0.749169

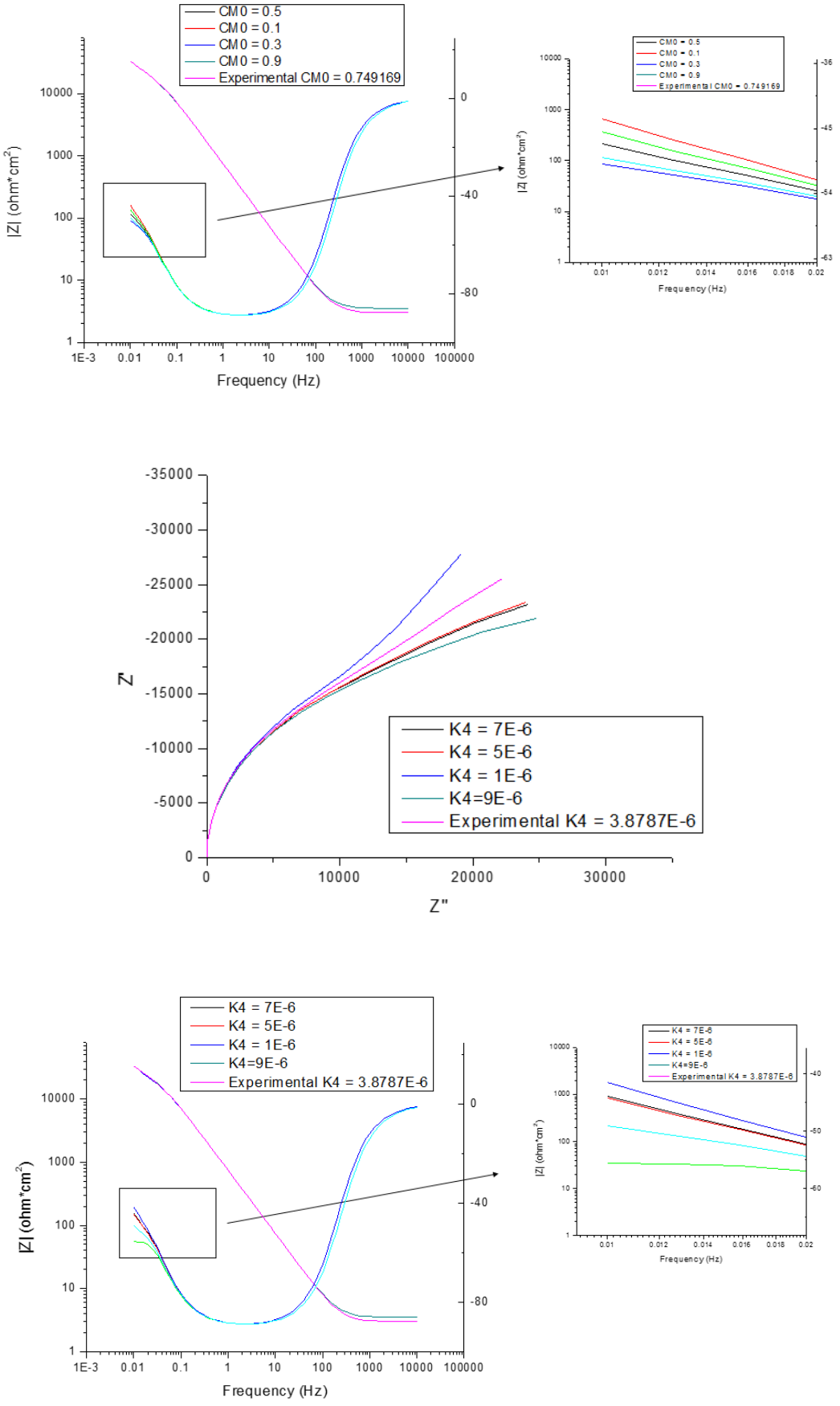

Figure 5.11 Sensitivity analyses for variables α_1, α_2, C_i^L, C_m^0, and k_4.

Figure 5.11 shows the sensitivity analysis for the variables of importance to the model. The transfer coefficient for reactions 1 and 4 appears to be the most sensitive variable of the model. Indeed, the transfer coefficient would greatly modify the end result and response to EIS at steady state and modify the spatial configuration of the bi-layer system. The reaction rate constant for reaction 4 was also sensitive to the model, which is to be expected since the rate of production of cation vacancies would eventually lead to a faster charge transfer process that modifies the EIS response. The dimensionless concentration of cation vacancies at the metal/barrier layer interface did not modify the expected behavior as much; considering that the maximum concentration differential is when the value reaches zero, the fact that the response does not change at much is advantageous since the movement of vacancies will be mostly the same through the nanoscale-thick barrier layer. The same argument can be applied for the metal interstitials; in addition, the barrier layer being predominantly p-type would not be affected as much by the n-type reaction types.

5.5 Summary of chapter

In this chapter, a study of the electrochemical performance of UNS S32003 in a 1.0 M NaCl solution environment was performed by means of AC techniques. Microscopy and XPS techniques were also used to characterize the corrosion type and the passive layer, respectively. A PDM was proposed for simulating the electrochemical behavior of the metal/passive layer/electrolyte interface to reproduce the experimental data and explain the surface oxidation reactions.

A chromium-containing oxide layer of approximately 2 nm was found adjacent to the substrate; this layer is considered responsible for the passivity and protection of the

metal. Another iron-rich layer of even smaller thickness can be found at the outermost location of the metal. A PDM of two layers was proposed.

The PDM proposed included several assumptions, such as the iron reacting with chromium vacancies in the barrier layer, allowing it to annihilate the vacancy and transporting the iron species to the barrier layer/outer layer interface where it can replenish and grow the outermost iron-rich oxide layer.

High concentrations of cation vacancies increase the likelihood of pitting corrosion initiation. The most severe environment in this regard was 0.5 M NaCl solution.

The results of the PDM values are analogous to equivalent circuits obtained in chapter three from EIS; however, the application of the PDM yields results from thermodynamic data, obtainable from deterministic equations which allow for a more thorough evaluation of the performance of the alloy/system than electrical values alone.

REFERENCES

[1] P. R. Rhodes, “Environment-assisted cracking of corrosion-resistant alloys in oil and gas production environments: a review,” *Corrosion*, vol. 57, no. 11, pp. 923–966, 2001.

[2] T. Mackenzie, “ATI 2003® Lean Duplex for Oil and Gas Structural Applications.”

[3] R. F. A. Jargelius-Pettersson, “Application of the pitting resistance equivalent concept to some highly alloyed austenitic stainless steels,” *Corrosion*, vol. 54, no. 2, pp. 162–168, 1998.

[4] R. Gunn, *Duplex stainless steels: microstructure, properties and applications*. Elsevier, 1997.

[5] D. Eliezer, D. G. Chakrapani, C. J. Altstetter, and E. N. Pugh, “The influence of austenite stability on the hydrogen embrittlement and stress-corrosion cracking of stainless steel,” *Metall. Trans. A*, vol. 10, no. 7, pp. 935–941, 1979.

[6] J. J. DUNN and D. S. BERGSTROM, “Development of a new lean duplex stainless steel, AL 2003 Alloy (UNS S32003),” *Stainl. steel world*, vol. 15, no. DEC, pp. 44–49, 2003.

[7] D. D. Macdonald, S. R. Biaggio, and H. Song, “Steady-State Passive Films Interfacial Kinetic Effects and Diagnostic Criteria,” *J. Electrochem. Soc.*, vol. 139, no. 1, pp. 170–177, 1992.

[8] P. Marshall, *Austenitic stainless steels: microstructure and mechanical properties*. Springer Science & Business Media, 1984.

[9] D. D. Macdonald, “The point defect model for the passive state,” *J. Electrochem. Soc.*, vol. 139, no. 12, pp. 3434–3449, 1992.

[10] I. Nicic and D. D. Macdonald, “The passivity of Type 316L stainless steel in borate buffer solution,” *J. Nucl. Mater.*, vol. 379, no. 1, pp. 54–58, 2008.

[11] R. De Gryse, W. P. Gomes, F. Cardon, and J. Vennik, “On the Interpretation of Mott-Schottky Plots Determined at Semiconductor/Electrolyte Systems,” *J. Electrochem. Soc.*, vol. 122, no. 5, pp. 711–712, 1975.

[12] C. Y. Chao, L. F. Lin, and D. D. Macdonald, “A point defect model for anodic passive films I. Film growth kinetics,” *J. Electrochem. Soc.*, vol. 128, no. 6, pp. 1187–1194, 1981.

[13] “ASTM G61 - 86(2014) Standard Test Method for Conducting Cyclic Potentiodynamic Polarization Measurements for Localized Corrosion Susceptibility of Iron-, Nickel-, or Cobalt-Based Alloys,” *ASTM*, 2003.

[14] “ASTM G 150 (1999). Standard Test Method for Electrochemical Critical Pitting Temperature Testing of Stainless Steels.,” *ASTM*, 1999.

[15] T. Piao and S. Park, “Spectroelectrochemical studies of passivation and transpassive breakdown reactions of stainless steel,” *J. Electrochem. Soc.*, vol. 144, no. 10, pp. 3371–3377, 1997.

[16] B. Ozturk, J. J. Dunn, and J. F. Grubb, “Corrosion Properties of Duplex Stainless UNS S32003 Alloy,” *Corros. 2008*, 2008.

[17] D. Wallinder, J. Pan, C. Leygraf, and A. Delblanc-Bauer, “EIS and XPS study of surface modification of 316LVM stainless steel after passivation,” *Corros. Sci.*, vol. 41, no. 2, pp. 275–289, 1998.

[18] M. Sánchez, J. Gregori, C. Alonso, J. J. García-Jareño, H. Takenouti, and F. Vicente, “Electrochemical impedance spectroscopy for studying passive layers on steel rebars immersed in alkaline solutions simulating concrete pores,” *Electrochim. Acta*, vol. 52, no. 27 SPEC. ISS., pp. 7634–7641, 2007.

[19] M. Da Cunha Belo, M. Walls, N. E. Hakiki, J. Corset, E. Picquenard, G. Sagon, and D. Noël, “Composition, structure and properties of the oxide films formed on the stainless steel 316L in a primary type PWR environment,” *Corros. Sci.*, vol. 40, no. 2, pp. 447–463, 1998.

[20] G. J. Brug, A. L. G. Van Den Eeden, M. Sluyters-Rehbach, and J. H. Sluyters, “The analysis of electrode impedances complicated by the presence of a constant phase element,” *J. Electroanal. Chem. interfacial Electrochem.*, vol. 176, no. 1, pp. 275–295, 1984.

[21] D. R. Baer, M. H. Engelhard, a. S. Lea, P. Nachimuthu, T. C. Droubay, J. Kim, B. Lee, C. Mathews, R. L. Opila, L. V. Saraf, W. F. Stickle, R. M. Wallace, and B. S. Wright, “Comparison of the sputter rates of oxide films relative to the sputter rate of SiO[sub 2],” *J. Vac. Sci. Technol. A Vacuum, Surfaces, Film.*, vol. 28, no. 5, p. 1060, 2010.

[22] S. J. Kerber and J. Tverberg, “Stainless steel: surface analysis,” *Adv. Mater. Process.*, vol. 158, no. 5, pp. 33–36, 2000.

[23] S. Ahn, H. Kwon, and D. D. Macdonald, “Role of chloride ion in passivity breakdown on iron and nickel,” *J. Electrochem. Soc.*, vol. 152, no. 11, pp. B482–B490, 2005.

[24] P. C. Pistorius and G. T. Burstein, “Metastable pitting corrosion of stainless steel and the transition to stability,” *Philos. Trans. R. Soc. London. Ser. A Phys. Eng. Sci.*, vol. 341, no. 1662, pp. 531–559, 1992.

[25] G. S. Frankel, L. Stockert, F. Hunkeler, and H. Boehni, “Metastable pitting of stainless steel,” *Corrosion*, vol. 43, no. 7, pp. 429–436, 1987.

[26] H. J. Engell, “Stability and breakdown phenomena of passivating films,” *Electrochim. Acta*, vol. 22, no. 9, pp. 987–993, 1977.

[27] J. Kruger, “The nature of the passive film on iron and ferrous alloys,” *Corros. Sci.*, vol. 29, no. 2, pp. 149–162, 1989.

[28] J. Liu and D. D. Macdonald, “The passivity of iron in the presence of ethylenediaminetetraacetic acid. II. The defect and electronic structures of the barrier layer,” *J. Electrochem. Soc.*, vol. 148, no. 11, pp. B425–B430, 2001.

[29] V. D. F. Cunha Lins, M. L. Magalhães Ferreira, and P. A. Saliba, “Corrosion Resistance of API X52 Carbon Steel in Soil Environment,” *J. Mater. Res. Technol.*, vol. 1, no. 3, pp. 161–166, Oct. 2012.

[30] M. D. C. Belo, N. E. Hakiki, and M. G. S. Ferreira, “Semiconducting properties of passive films formed on nickel–base alloys type Alloy 600: influence of the alloying elements,” *Electrochim. Acta*, vol. 44, no. 14, pp. 2473–2481, 1999.

[31] K. W. Frese, M. J. Madou, and S. R. Morrison, “Investigation of Photoelectrochemical Corrosion of Semiconductors II. Kinetic Analysis of Corrosion-Competition Reactions on,” *J. Electrochem. Soc.*, vol. 128, no. 7, pp. 1527–1531, 1981.

[32] M. F. Montemor, M. G. S. Ferreira, N. E. Hakiki, and M. D. C. Belo, “Chemical composition and electronic structure of the oxide films formed on 316L stainless steel and nickel based alloys in high temperature aqueous environments,” *Corros. Sci.*, vol. 42, no. 9, pp. 1635–1650, 2000.

[33] C. L. Nguyen and J. B. Metson, “Differential sputtering and the formation of repeating fragments in ToF-SIMS spectra of light metal alloy surfaces,” *Surf. Interface Anal.*, vol. 45, no. 1, pp. 449–452, 2013.

[34] A. M. P. Simoes, M. G. S. Ferreira, B. Rondot, and M. da Cunha Belo, “Study of passive films formed on AISI 304 stainless steel by impedance measurements and photoelectrochemistry,” *J. Electrochem. Soc.*, vol. 137, no. 1, pp. 82–87, 1990.

[35] Y. Chen, M. Urquidi-Macdonald, and D. D. Macdonald, “The electrochemistry of zirconium in aqueous solutions at elevated temperatures and pressures,” *J. Nucl. Mater.*, vol. 348, no. 1, pp. 133–147, 2006.

[36] D. D. Macdonald, “Passivity–the key to our metals-based civilization,” *Pure Appl. Chem.*, vol. 71, no. 6, pp. 951–978, 1999.

APPENDIX

FITTING PROCEDURE.

```
//Functions listed here are Explicitly for version 2.1 of Ellis.  Each function has a
setup function and an executable fit function.

#pragma rtGlobals=3             // Use modern global access method.


Menu "Ellis2"

        Submenu "1. Run your setup function"

                "1.1 Setup Randles", setupZrandles()

                "1.2 Setup QPE", setupZqandles()

                "1.3 Setup QPE + Warburg", setupZqandlesW()

                "1.4 Setup Randles + Warburg", setupZrandlesW()

                "1.5 Setup Randles2", setupZrandles2()

                "1.6 Setup Qandles2", setupZqandles2()
```

```
                "1.7 Setup Qandles + Porous Bounded Warburg", setupZqandlesB()

                "1.8 Setup Qandles + Bounded Warburg", setupZqandlesT()

                "1.9 Setup Qandles2 parallel", setupZqandles2P()

                "1.10 Setup Reduced transmission line", setupZunifiedtline0()

                "1.11 Setup balanced transmission line", setupZunifiedtlineC()

//              "1.12 Jean",setupZ

                "1.X Setup user function", Execute/q "setup"+testsetupvals[0]+"()"

                "1.13 setup PDM Javier", setupZpdm()

                "1.14 setup PDM Javier Simple", setupZpdmsimple()

                "1.15 setup PDM Javier Diffusion", setupZpdmdiffusion()

        End

End


Function setupZpdmMarx()
```

```
	Make/O/D limits
={{0,0,0,0,0,0,0,1000000,0,0,0,0,0,0,0,0,0,0,0,0,0,0,0},{1,1,1,1,1,1,1,1000000,1,1,1
,1,1,1,1,1,1,1,1,10000,5,5,50,1}}		// make the lower and upper limits

	Make/O/D coefs =
{.5,.5,.5,.5,.5,.5,.5,1000000,.5,.5,.5,.5,.5,.5,.5,.5,.5,.5,.5,100,.5,.5,.5,5,0}		//
make the initial coefficients

	make/T/O
coeffnames={"alpha1","alpha2","alpha3","alpha4","alpha5","alpha7","alpha","eps","
Cbl","K1","K2","K3","K4","K5","K7","CHN","CM0","CIL","ohm","Rol","x","d","R
E","Col"}	// make a list of coefficient names

	make/O/I/N=(numpnts(coefs)) heldlist=0		// 0 = not held.  1 = held.
(during fit)

	string/g currentmodel="ZpdmMarx"

	wave/t testsetupvals

	testsetupvals[0]="ZpdmMarx"

	make/t/o tempwavenames={"complexer","a1","a2","a3","a4","a5", "a7",
"LV", "LI", "CIVL", "CIIL", "CMV0", "CMI0","IV", "II","IL",
"IM0","IIL","F","RG","TE","b1","b2","b3"}

	preflight1()

End
```

```
Threadsafe Function ZpdmMarx(w,complexcat,freqw): fitfunc

	wave complexcat, w, freqw //declare wave names.  Don't edit this

	wave/c
complexer,a1,a2,a3,a4,a5,a7,LV,LI,CIVL,CIIL,CMV0,CMI0,IV,II,IL,IM0,IIL,F,RG,
TE,b1,b2,b3

	variable/g midpointt

	variable/g/c ki //pull in complex constant

	variable
alpha1,alpha2,alpha3,alpha4,alpha5,alpha7,alpha,eps,Cbl,K1,K2,K3,K4,K5,K7,CHN,
CM0,CIL,ohm,Rol,x,d,RE,Col //declare variable names; you can edit this



	alpha1=w[0]//alpha1

	alpha2=w[1]//alpha2

	alpha3=w[2]//alpha3

	alpha4=w[3]//alpha4

	alpha5=w[4]//alpha5

	alpha7=w[5]//alpha7
```

alpha=w[6]//polarization coefficient

eps=w[7]//electric field

Cbl=w[8]//Cbl

K1=w[9]//K1

K2=w[10]//K2

K3=w[11]//K3

K4=w[12]//K4

K5=w[13]//K5

K7=w[14]//K7

CHN=w[15]//CHN

CM0=w[16]//CM0

CIL=w[17]//CIL

ohm=w[18]//ohm

Rol=w[19]//Rbl

x=w[20]//x

d=w[21]//d

RE=w[22]//RE

Col=W[23]//Col

F= 96485

RG= 8.314

TE= 298.15

a1 = x*alpha1*(1-alpha)*F/(RG*TE)

a2 = x*alpha2*(1-alpha)*F/(RG*TE)

a3 = x*alpha3*(1-alpha)*F/(RG*TE)

a4 = (d-x)*alpha4*alpha*F/(RG*TE)

a5 = (d-x)*alpha5*alpha*F/(RG*TE)

a7 = (d-x)*alpha7*alpha*F/(RG*TE)

b1 = x*alpha1*eps*F/(RG*TE)

b2 = x*alpha2*eps*F/(RG*TE)

b3 = x*alpha3*eps*F/(RG*TE)

IV = F*(x*K1*a1*CM0 + x*K2*a2 + x*K3*a3 + (d-x)*K4*a4 + (d-x)*K5*a5*CIL + (d-x)*K7*a7*CHN)

IL = -F*(x*K1*b1*CM0 + x*K2*b2 + x*K3*b3)

II = -Rol*IV

IM0 = F*(x*K1)

IIL = F*(d-x)*K5

LV = ohm*(K3*a3 - K7*a7*CHN)/(ki*freqw+ohm*K3*b3)

LI = - LV*Rol

CIVL = K2*a5/(ki*freqw + K5)

CIIL = -CIVL*Rol

CMV0 = K4*a1/(ki*freqw+K1)

CMI0 = -CMV0*Rol

complexer[0,midpointt-1]= RE + 1/((ki*freqw*Cbl) + (IV+IL*LV + IIL*CIVL + IM0*CMV0)/(1-(II - IL*LI + IIL*CIIL + IM0*CMI0))) + 1/((1/Rol) + ki*freqw*Col)

complexcat[0,midpointt-1]=real(complexer[p]) // don't edit this line. Writes real part to complexcat first half

complexcat[midpointt,]=imag(complexer[p-midpointt]) //don't edit this line. Writes imaginary part to complexcat second part

End.